

Octopi: Open configurable high-throughput imaging platform for infectious disease diagnosis in the field

Hongquan Li¹, Hazel Soto-Montoya^{2†}, Maxime Voisin^{3†}

Lucas Fuentes Valenzuela^{1†}, Manu Prakash.^{3*}

¹Department of Electrical Engineering, ²Department of Bioengineering,

³Department of Computer Science

Stanford University, Stanford, CA

† Equal contribution

*To whom correspondence should be addressed; E-mail: manup@stanford.edu

June 26, 2019

ABSTRACT

Access to quantitative, robust, yet affordable diagnostic tools is necessary to reduce global infectious disease burden. Manual microscopy has served as a bedrock for diagnostics with wide adaptability, although at a cost of tedious labor and human errors. Automated robotic microscopes are poised to enable a new era of smart field microscopy but current platforms remain cost prohibitive and largely inflexible, especially for resource poor and field settings. Here we present *Octopi*, a low-cost (\$250-\$500) and reconfigurable autonomous microscopy platform capable of automated slide scanning and correlated bright-field and fluorescence imaging. Being highly modular, it also provides a framework for new disease-specific modules to be developed. We demonstrate the power of the platform by applying it to automated detection of malaria parasites in blood smears. Specifically, we discovered a spectral shift on the order of 10 nm for DAPI-stained *Plasmodium falciparum* malaria parasites. This shift allowed us to detect the parasites with a low magnification (equivalent to 10x) large field of view (2.56 mm²) module. Combined with automated slide scanning, real time computer vision and machine learning-based classification, *Octopi* is able to screen more than 1.5 million red blood cells per minute for parasitemia quantification, with estimated diagnostic sensitivity and specificity exceeding 90% at parasitemia of 50/ul and 100% for parasitemia higher than 150/l. With different modules, we further showed imaging of tissue slice and sputum sample on the platform. With roughly two orders of magnitude in cost reduction, *Octopi* opens up the possibility of a large robotic microscope network for improved disease diagnosis while providing an avenue for collective efforts for development of modular instruments.

One sentence summary: We developed a low-cost (\$250-\$500) automated imaging platform that can quantify malaria parasitemia by scanning 1.5 million red blood cells per minute.

Keywords: automated modular microscope, malaria diagnosis, low-cost instruments, machine learning

1 Introduction

2 Lack of cost-effective diagnostics is a major hurdle in global fight against infectious disease,
3 specially in resource poor settings [1]. This leaves our world in a highly vulnerable position
4 with therapeutic drugs being either overused, leading to drug resistant strains or not acces-
5 sible to people who actually need these treatments [2]. Since health care is delivered around
6 the world in a tiered structure, local context such as high cost, lack of trained personal or
7 low throughput of many available diagnostics tests plays a large detrimental role on quality
8 of delivered health-care [3].

9 Because of the versatility and wide adoption of manual microscopy [4] and its role in
10 direct visual identification of parasites [5], it remains a WHO gold standard for numerous
11 diseases [1]. Despite technological advancements in related fields, the practice of conventional
12 manual microscopy has remained largely unchanged over the last half century and suffers
13 from several drawbacks. With an average lab technician spending 6 to 8 hours imaging and
14 examining slides per day, human fatigue has been identified as a crucial factor in reduced
15 efficiency in microscopy based diagnostics [6]. With heavy disease burden, number of patient
16 samples that need to be processed, even at small primary health centers, can often supersede
17 the capacity of laboratory workers [7]. The above listed limitations for microscopy are not
18 fundamental, and can be circumvented with field implementation of low-cost, motorized
19 microscopes combined with computer-based automated detection.

20 Low-cost field microscopy has made tremendous strides in the last decade [8], both to-
21 wards access and implementing application-specific capabilities [9, 10, 11, 12, 13, 14]. New
22 microscopy techniques such as Fourier ptychographic microscopy [15] and lens-free on-chip
23 microscopy [16, 17, 18] have also been developed to tackle some of the hurdles of conven-
24 tional microscopy in diagnostics settings. These platforms and techniques have demonstrated
25 a wide range of applications [19, 20] but high throughput diagnosis of malaria has remained
26 out of reach.

27 Despite all the resources invested, malaria remains to be a highly deadly disease. In

28 the year of 2017, there were 219 million cases and nearly 435,000 deaths, majority of them
29 occurring due to *Plasmodium falciparum*, a strain of malaria widely spread across the world
30 [21]. Two most widely used diagnostic tests are antigen-based Rapid Diagnostic Test (RDT)
31 and microscopic examinations of blood smears. In the same year, 276 million RDTs were sold
32 and more than 208 million patients were tested by microscopy, whereas estimated needs for
33 testing was well over 1 billion [22]. While RDT is easy to use, it cannot quantify parasitemia,
34 stays positive post treatment for up to a month [23] and can create false negative due to
35 HRP2/3 gene deletions [24, 25]. Manual microscopy, on the other hand, is labor intensive and
36 in practice the performance is often compromised. Commercial slide scanning and detection
37 systems show promise [26, 27] but are currently expensive. With persisting high burden of
38 malaria [28] and the rise of drug resistance strains [29, 30, 31], affordable, high-throughput
39 and quantitative diagnostic tests are urgently needed.

40 Here we present *Octopi*, a low-cost (\$250-\$500), portable (below 3 kg), reconfigurable and
41 automated imaging platform for disease diagnosis in resource constrained settings. To enable
42 versatility of the platform and its adoption for different diseases, we take a highly modular
43 approach where the platform can be configured with different disease-specific modules. On
44 this platform, we demonstrate automated slide scanning with multimodal imaging with two
45 imaging heads that support a range of magnifications.

46 In particular, we report a spectral shift on the order of 10 nm for DAPI-labeled *P.*
47 *falciparum* malaria parasites when compared to often confounding DAPI-labeled platelets in
48 patient samples. This discovery enables us to integrate three channels of information (bright-
49 field, fluorescence and spectral) for automated detection of *P. falciparum* parasites with a low
50 magnification imaging module. Large field of view afforded by this module, combined with
51 automated slide scanning and image processing, allows screening of more than 1.5 million
52 red blood cells per minute for infections, which is 120 times faster compared to traditional
53 manual microscopy [32]. We further implement a machine learning classifier and obtain
54 anticipated performance of higher than 90% specificity and sensitivity for parasitemia of 50

55 parasites per μl and 100% sensitivity and specificity for parasitemia of 150 parasites per μl .
56 Our results suggest that low-cost automated multimodal microscopy combined with machine
57 learning tools have the potential to address the unmet needs for diagnosis of malaria and
58 many other diseases.

59 **Results**

60 **Automated imaging platform with modular design**

61 The imaging platform consists of completely separable modules that fall into 5 categories:
62 imaging, slide scanning, transillumination, oblique angle laser illumination and control &
63 computation (Fig. 1A). When setting up the imaging platform (Fig. 1B), preassembled
64 modules snap to each other due to embedded magnets (see mounting of the imaging head
65 in Movie S1 for example). Since screws are not necessary for the connections, the imaging
66 platform can be rapidly reconfigured.

67 We designed the platform with a combination of standard and custom parts, with choices
68 being made to optimize performance, size, cost, and ease in prototyping and iterative devel-
69 opment. For example, we made the imaging and transillumination module compatible with
70 the standard cage and lens tube system, which allowed us to quickly implement different
71 configurations. For the custom parts that form the backbone of the microscope, we chose
72 CNC machining with 6061 aluminum over other manufacturing options for the rigidity of
73 metal, the tight tolerance of the machining process and the low surface roughness of the
74 finished parts. CNC machining also has favorable cost-volume scaling: at the manufacturing
75 quantity of 10, the price is already comparable with 3D printing.

76 To facilitate wide adoption of the imaging platform, including in resource limited settings,
77 cost is imposed as an important design constraint during development. Through careful
78 choices of parts and their arrangements, we were able to keep the starting unit cost of the
79 imaging platform to about \$700 for volume of 10 units. Without significantly altering the

80 design, the cost reduces to \$350 for volume of 100 units and \$250 for volume of 1000 units
81 (table S1).

82 **The imaging modules**

83 We implemented two different imaging modules, one with low magnification (*low mag imag-*
84 *ing module*) and one with high magnification (*high mag imaging module*). The *low mag*
85 *imaging module* is based on the reversed lens configuration, where two multi-element cell-
86 phone lenses are used as objective and tube lens in the infinity-corrected configuration [33].
87 To enable fluorescence imaging, an interference long pass filter diced into the size of 3 mm x 3
88 mm can be placed in between the two lenses (Fig. 1A inset). The CMOS sensor (Pi Camera
89 based on Sony IMX219), lenses and optional filter are assembled around a CNC machined
90 part as a permanent assembly. Because the cost of the parts is low, for different filters or
91 lens combinations, different permanent assembly can be made. This eliminates the needs
92 for users to handle small and intricate parts and helps keep the optical train free from dusts
93 and contamination. The f-number of the lenses used in our implementation is 2.0, which
94 translates to numerical aperture of 0.25, typical of 10X objectives. With condenser-based
95 transillumination for bright field and oblique angle laser illumination for fluorescence, we
96 got Nyquist-limited resolution of $2.5 \mu m$ (2.3 times the object side pixel size) over field of
97 view of more than 1.6mm x 1.6mm (Fig. 2A). By using different pairs of lenses, diffraction
98 limited resolution ($0.92 \mu m$) of a 10X/0.3NA objective lens may be achieved.

99 The *high mag imaging module* makes use of standard infinity-corrected microscope ob-
100 jectives. Depending on required sensitivity and frame rate, Pi Camera or standard industrial
101 camera may be used, with M12 lens or C-mount imaging lens acting as tube lens. Notably,
102 with starting price below \$100, industrial cameras with low light CMOS sensors can offer
103 peak quantum efficiency of more than 70% and readout noise as low as 1.1 e- (see Fig. S1),
104 rivaling the performance of high-end scientific cameras. Using Pi Camera, a $f = 25\text{mm}$ M12
105 lens and a 40x/0.65 Plan Achromatic objective, with the same illumination used for the low

106 mag module, Nyquist-limited resolution of $0.46 \mu\text{m}$ can be achieved with field of view of
107 $0.4\text{mm} \times 0.4\text{mm}$ (Fig. 2B).

108 High-throughput automated imaging requires robust auto-focus. In the *low mag imaging*
109 *module* we implemented motorized focusing with a captive linear actuator. The step size of
110 the linear actuator is $1.5 \mu\text{m}$, which is sufficiently small compared to the depth of focus of
111 more than $8 \mu\text{m}$. Motorized focus adjustment for the *high mag imaging module* has more
112 stringent requirements, given the depth of focus is as small as $1 \mu\text{m}$ for a 40x/0.65 objective.
113 As a solution, we combined a low-cost piezo stack actuator and a standard linear translation
114 stage with extended contact ball bearings/crossed roller bearings. The piezo stack actuator
115 used has travel of $11.2 \mu\text{m}$ and step size of 2.73nm when used with a 12-bit digital to analog
116 converter (see movie S2 for demo of focus actuation with this implementation). To test the
117 performance of the motorized focus actuation for the low and high mag module, we acquired
118 series of z-stacks of blood smears and plotted the computed focus measures vs the commanded
119 z-position (Fig. 2 C,D). That the curves lie on top of each other indicates excellent reliability
120 and repeatability. Utilizing the dependence of focus measure on z position, we implemented
121 contrast-based auto-focus. Alternatively, with small modifications in illumination, different
122 single-shot focus-finding approaches [34, 35] can be used for faster focus.

123 **Illumination modules**

124 The bright field transillumination module consists of a LED panel, a diffuser and an NA
125 $= 0.79$ condenser. The diffuser is placed at the focal plane of the condenser to make the
126 illumination Kohler-like. Dark-field illumination for low magnification can be provided simply
127 by a ring of LED, while an LED matrix can be used for quantitative phase imaging, fourier
128 ptychography [15, 36] and single-shot auto-focus [34, 35]. For fluorescence excitation, we
129 make use of oblique angle laser illumination [9]. Used in a wide range of consumer electronics
130 such as Blu-Ray/DVD/CD players, projectors and laser pointers, direct diode laser and
131 diode-pumped solid state lasers that can provide tens to hundreds of mWs optical power are

132 available at a wide range of wavelengths at very low cost. Currently, available wavelengths
133 include 405 nm, 450 nm, 465 nm, 505 nm, 520 nm, 532 nm, 635nm, 650 nm, 780 nm, 808 nm,
134 1064 nm. Because of the monochromatic nature of the laser, no excitation filter is needed.
135 The use of oblique angle illumination also eliminates the need for dichroic beam splitter,
136 reducing both the overall size and the cost of the setup. In addition, multiple lasers can be
137 used and electronically switched for multiplexing.

138 **The scanning module**

139 Motorized slide scanning is crucial for high throughput imaging. Commercial motorized
140 stage for microscopes offers incremental motion as low as a few nanometers but typically
141 cost thousands of US dollars. Realizing that for wide field imaging such level of positioning
142 performance is not needed, we developed a low cost scanning module using lead screw linear
143 actuator that costs as little as \$5 per unit. A important performance criterion is the scan
144 flatness, which is the relative z-displacement of the slide at the center of the microscope field
145 of view as the slide is being scanned. Good flatness reduces the need for frequent auto-focus.
146 To ensure good scanning flatness, in our present configuration, the slide rests directly on
147 a CNC machined block and is moved by a slide scanner driven by the lead screw linear
148 actuators. To characterize our stage flatness, we used an ultra-flat quartz coated glass slide
149 (and in another measurement, a normal microscope glass slide) as target and measured with
150 a non-contact sensor the displacement of its top surface as it is being scanned (Fig. S2). The
151 result (Fig. 2E, Fig. S3), which is limited by measurement setup, suggests overall flatness
152 below 400 nm over tens of millimeters.

153 **The control & computation module**

154 Raspberry Pi, a single board computer priced at \$35, provides a cost-effective way to control
155 the microscope. The linux operating system also makes it easy to take advantage of open
156 source software packages and simplifies development. In the Raspberry Pi-based implemen-

157 tation, the camera is interfaced using the industry standard MIPI camera serial interface,
158 whereas other components are controlled through driver boards and MOSFET switches.

159 With increasing demands for artificial intelligence at the edge, various low-cost and
160 energy-efficient ASIC chips and embedded systems with optimized hardware for computer
161 vision and machine learning applications have recently emerged. For applications requiring
162 more compute power and/or higher imaging throughput, these platforms can be adopted. In
163 particular, we have implemented and tested image processing and spot detection pipelines on
164 Jetson Nano, a \$99 drop-in replacement for Raspberry Pi with 128 CUDA cores. This imple-
165 mentation reduces processing time by more than 50 times and allows processing to be done in
166 real time as slides are being scanned (Fig. S4). Further more, when Windows-only software
167 needs to be used, or more compute power is required, laptops or desktop workstations can
168 also be used.

169 **Power consumption**

170 When Raspberry Pi or Jetson Nano are used as the control & computation module, the
171 entire system can be powered from 5V DC power supplies. Either a wall plug AC adapter
172 or a battery pack may be used. For a battery pack with capacity of 20,000 mAh, a single
173 charge can power the microscope for more than 8 hours of continuous use (assuming full
174 power consumption).

175 **Automated blood smear examination**

176 Blood smear examination is commonly used for diagnosing blood-borne diseases and often
177 requires imaging many microscopic field of views. *Octopi* as a high-throughput imaging
178 platform is particularly suited for these applications. To use the platform, stained blood
179 smear is prepared following the same protocol used for manual microscopy (Fig. 3A). The
180 slide is then loaded to the imaging platform and scanned automatically. For samples stained
181 with fluorescent dyes, in addition to bright field image, a fluorescent image is also taken for

182 each field of view, during which the LED is switched off and the laser is switched on by the
183 controller (movie S1).

184 Because of the absence of nucleus in red blood cells, fluorescent dyes that bind to the
185 nucleic acid may be used for staining platelets, white blood cells and many parasites in
186 blood smears with improved contrast compared to bright field stains. The dark field nature
187 of fluorescence imaging also makes it possible to localize stained objects that are below the
188 diffraction limit of the objective being used. This allows us to use low magnification optics
189 that have lower resolutions but larger field view, resulting in higher imaging throughput. Fur-
190 thermore, in fluorescent imaging, since angular distribution of emitted light is independent
191 of illumination, full numerical aperture of the objective is automatically utilized.

192 Among many fluorescent nucleic acid dyes, 4',6-diamidino-2-phenylindole (DAPI) has
193 several attractive properties, including 20-fold fluorescence enhancement upon binding to
194 the AT-region of dsDNA, low-cost (staining a blood smear costs less than \$0.02 without
195 reusing the staining solution), and good temperature stability. According to published data
196 sheet [37], DAPI solutions are stable at room temperature for 1 to 2 weeks [38] and at
197 +4°C for up to 6 month. In practice, we got similar staining results with DAPI solution (at
198 staining concentration of 5 $\mu\text{g}/\text{ml}$) left in the dark at room temperature for several months.
199 To demonstrate the use of DAPI with the *low mag imaging module* on our platform, we
200 scanned a smear of whole blood that is stained in DAPI solution for one minute. In the
201 resulting images, not only white blood cells, but also reticulocytes and platelets can be
202 easily resolved (Fig. 3B).

203 To be able to robustly extract fluorescent spots for quantification, we developed a two-
204 step processing pipeline (Fig. S5). The first step uses top-hat transformation to remove
205 background. The second step uses a blob detector based on the Laplacian of Gaussian
206 (LoG) [39, 40] to detect fluorescent spots of different sizes and intensities. Since filtering
207 operations involved in both steps are computationally expensive for CPUs, we implemented
208 a version of the pipeline that takes advantage of CUDA cores in GPU. When deployed on

209 Jetson Nano for detecting platelets (and later, also malaria parasites), we're able to get per
210 image processing time of around 300 ms, which is more than 50 times faster compared to
211 using a Raspberry Pi 3B+ and 5 times faster compared to using desktop computers (Fig.
212 S4). With scanning speed of 1 field of view per second, this allows equivalent blood smear
213 examination throughput of 3,000,000 red blood cells (or 0.6 μ l blood) per minute (assuming
214 red blood cells cover 75% area of the field of view).

215 Directly counting red blood cells can be beneficial for quantitative analysis of the blood
216 and for determining parasitemia in the case of infection, especially when the precise volume
217 of blood being smeared is not known. However, at low magnification, when cells are only
218 stained with fluorescent dyes, segmentation becomes challenging. In particular, because each
219 red blood cell has only 5-7 pixels in diameter and the contrast is not uniform across the cell,
220 simple thresholding or edge detection-based methods do not work well. Hough transforms
221 used for detecting circular objects requires the image to be scaled up, which leads to sig-
222 nificant processing overhead, and has trouble detecting red blood cells that have distorted
223 shapes. To address this challenge, we trained a 91-layer fully convolutional DenseNet [41],
224 which gives good performance (Fig. 3C, Fig. S6). By compressing the model through
225 pruning, quantization and other optimizations [42] and deploying it on Jetson Nano, real-
226 time performance can be expected. To further improve throughput, more lightweight model
227 [43, 44] may be trained and ASIC chips may be used [45].

228 To demonstrate use case for detecting larger parasites using only bright-field imaging,
229 we digitized a Giemsa-stained blood smear with Loa-Loa parasites (Fig. 3(D)). Because
230 the parasite can be identified unambiguously, blood volume limited-detection limit of 0.2-0.5
231 parasites/ μ l can be achieved. This detection threshold is well below the Sever Adverse Effect
232 (SAE) threshold of 30 parasites/ μ l, above which mass drugs should not be administrated to
233 the individual patient [12]. For screening this particular parasite, video microscopy [12] has
234 also been used and can be configured on *Octopi* to further improve throughput.

235 The advantage of automated scanning becomes evident by examining the probability

236 of occurrence of a given number of parasites in scanned fields of view. For a hypothetical
237 parasitemia of 100 parasites/ μ l, we plot the probability of more than 10 parasites being
238 present as a function of number of fields of views scanned for two different magnifications
239 (Fig. 3E). We can observe that if enough fields of views are examined, the probability goes to
240 one. Furthermore, in applications where the use of fluorescent dyes and/or pathogen-specific
241 probes renders the morphological features of the detection targets unimportant, or reduces
242 the requirement of optical resolution (such as in detecting DAPI-stained platelets), low
243 magnification can be used in place of high magnification to significantly boost throughput.
244 In the example above, to have at least 10 parasites with more than 95% probability, on
245 average only 16 low mag fields of view are needed, as compared to 1058 fields of views in
246 the case of 100 x oil objective. This calculation assumes that all the targets are in the same
247 plane. For targets that are distributed in 3D, such as in sputum sample or in tissue slices,
248 the increase in throughput is even more significant, given the depth of focus of 55 μ m, 8.8 μ m,
249 1.3 μ m and 0.53 μ m for 4x/0.1, 10x/0.25, 40x/0.65 and 100x/1.25 oil objectives.

250 **Automated detection of malaria parasites in thin blood smears**

251 Fluorescence microscopy has been used for sensitive detection of malaria parasites [46, 47, 48].
252 However the prospect of detection in fixed blood smears at low magnification is hindered
253 by the presence of brightly stained platelets, which are highly abundant (there are typically
254 250,000 platelets per μ l blood) and appear similarly in size and brightness as malaria para-
255 sites. Yet, *P. falciparum* malaria parasites, which have a 48-hour asexual life cycle, contain
256 not only DNA but also large amount of RNA. This provides an opportunity for differential
257 detection. Previously, it has been shown that the emitted fluorescence red-shifts in DAPI-
258 RNA complexes compared to DAPI-DNA complexes [49], which means that depending on
259 the DNA-RNA ratio cells, overall shift up to about 40 nm can be expected. In fact, this
260 property has been used in enumerating reticulocytes in rodent malaria models [50].

261 To support the feasibility of differentiating malaria parasites from platelets based on

262 DNA/RNA ratio and its associated spectral shift, we imaged smears of blood from healthy
263 individuals and patients diagnosed with malaria with laser scanning confocal microscopy
264 where spectrum at each pixel is recorded. The results revealed a spectral red shift on the
265 order of 10 nm for ring-stage *P. falciparum* parasites. For better visualization of the results,
266 we mapped the obtained 32-channel spectral stacks to pseudo color images (Fig. 4A, Fig. S7-
267 S8), where the color is determined by centroids of the spectrum, with purple being 485 nm or
268 below and yellow being 510 nm or above. Using the same color code, we plotted the spectrum
269 of selected spots (Fig. S8) in Fig. 4(B), where three clusters emerge. Examining the spots
270 (Fig. 4(C)) we can conclude that the first purple/dark blue cluster (centroid below 495 nm)
271 corresponds to platelets, and that the second green colored cluster (centroid at 495-500 nm)
272 belongs to ring-stage malaria parasites. Because of the absence of distinctive morphological
273 features, the identity of the third cluster where the “yellow” spectrum originate (centroid
274 above 505nm) remain to be determined. Likely candidates for the brighter “yellow” spots
275 include merozoites and trophozoites stages of the *P. falciparum* parasites, as these stages can
276 be stained intensively with RNA-selective dyes[51]. As they’re not observed in uninfected
277 blood, dimmer “yellow” spots can be accounted for by parasites-derived extracellular vesicles,
278 which have been reported to contain RNA and DNA[52, 53, 54, 55].

279 Traditionally, fluorescence microscopy is done with monochrome cameras and band pass
280 filter with relatively narrow pass band for better sensitivity and background suppression.
281 However, in doing so, spectral multiplexing will involve use of multiple filters or point spread
282 function engineering, which adds to the complexity of the system. Here by utilizing a long
283 pass filter and a color CMOS sensors where color filter arrays in the Bayer arrangements
284 are directly integrated on top of the pixels, we are able to obtain spectral information in a
285 single shot. To quantify the performance of this setup, we simulated the spots with spectrum
286 from the average of DAPI-stained platelets and DAPI-stained ring-stage parasites (Fig. 5A,
287 Fig. 5B). In the simulation, spots were assumed to have a Gaussian profile, and both
288 finite pixel size and photon shot noise were taken into account. To get a lower-dimensional

289 representation, the spots are then projected to normalized color space G/B vs R/B, where
290 R/B is the ratio of total red pixel intensity and total blue pixel intensity, and similarly G/B
291 is the ratio of total green pixel intensity and total blue pixel intensity (Fig. 5C). Intriguingly,
292 for spot sizes and signal levels easily achievable, spectral shift as low as 8 nm can result in
293 good separation in the G/B vs R/B space.

294 To show that our imaging platform configured with the *low mag imaging module* has
295 enough sensitivity for detecting DAPI-stained ring-stage parasites, we imaged the same smear
296 of *P. falciparum* culture on *Octopi* and on a high end research microscope (Nikon Ti2
297 with Prime 95B sCMOS sensor), and one-to-one correspondence of fluorescent spots can be
298 observed (Fig. 6A). Fig. 6B compares a typical overlaid bright-field and fluorescent field of
299 view of *P. falciparum* culture with that of uninfected whole blood, and the color difference
300 between parasites and platelets can be appreciated. To quantify how well parasites and
301 platelets may be told apart, we stained and imaged 8 smears of *P. falciparum* culture and
302 10 smears of uninfected whole blood, where a total number of 109,355 fluorescent spots from
303 the *P. falciparum* culture and 437,944 fluorescent spots from the uninfected whole blood
304 were detected and extracted using the aforementioned processing pipeline. Projection of
305 randomly selected 10,000 spots into the G/B vs R/B space is plotted in Fig. 6C. Good
306 separation in this scatter plot suggests and that color, as a manifestation of spectral shift,
307 is a robust feature for distinguishing parasites from platelets. The results also suggest the
308 absence of confounding objects in uninfected whole blood.

309 To automatically detect parasites from extracted spots and obtain diagnostic performance
310 that can be expected with the proposed solution, we built a boosted-tree classifier that takes
311 features from each extracted spots and outputs a class label. The performance of the classifier
312 can be characterized by its False Positive Rate (FPR) and False Negative Rate (FNR), where
313 FPR is the number of platelets misclassified as parasites over the total number of platelets
314 and FNR is the number of parasites misclassified as platelets over the total number of
315 parasites . We found that using combined features from bright-field images and fluorescent

316 images result in the best classification performance (Fig. 6D). Specifically, at FNR of 10%,
317 FPR of 0.05% (average of 20-fold cross validation, range is 0.027%-0.11%, standard deviation
318 is 0.019%) can be achieved. Because both declaration of a smear as negative and quantifying
319 parasitemia in the case of low parasitemia involves scanning a large area and counting a large
320 number of cells, and that brightly-stained platelets are highly abundant, it's important to
321 choose a decision threshold that gives relatively small per spot FPR. This lowers the chances
322 of misdiagnosing an uninfected case as infected and only has a weak negative influence on
323 sensitivity. With per spot $FPR = 5 \times 10^{-4}$ and $FNR = 11\%$, we obtain through Monte
324 Carlo simulations anticipated (per case) sensitivity and specificity of (91%,91%), (99%,99%)
325 and (100%,100%) for parasitemia of 50/ul, 100/ul and 150/ul (Fig. 6E). This simulation
326 assumes platelet count of 250,000/ul, all platelets being brightly labeled and that 0.5 μl
327 blood is screened. In the Jetson Nano-based implementation, the time it took from slide
328 being loaded to an answer (including parasitemia, in the case of infection) can be less than
329 2 minutes.

330 In certain cases it may be desirable to resolve the morphology of individual parasites.
331 This would further improve sensitivity and specificity, especially for cases with very low
332 parasitemia. This is made possible on our modular platform by using the *high mag imaging*
333 *module* with a 40x/0.65 objective. We imaged smears of uninfected whole blood (Fig. 7A),
334 lab culture of *P. falciparum* (Fig. 7B) and blood samples from patients diagnosed with
335 malaria (Fig. 7C). The result show that with morphology and/or color, parasites can be
336 easily told apart from platelets. Images of lab *P. falciparum* culture also confirm that many
337 parasites are indeed in their ring-stage, with presence of multiple infections, which is due to
338 the high concentration of parasites in the lab culture.

339 **Broader diagnostics applications**

340 Besides malaria, *Octopi* can be used to image a wide range of pathogens and conditions.
341 As examples, we imaged Schistosomiasis of human intesines tissue specimen (Fig. 8A),

342 *Leishmania donovani* that causes leishmaniasis (Fig. 8B), *Trypanosoma brucei rhodesiense*
343 (Fig. 8C) that causes African sleeping sickness, *Mycobacterium tuberculosis* that causes
344 tuberculosis (TB) (Fig. 8D), *Streptococcus pneumoniae* that can cause community-acquired
345 pneumonia (CAP) (Fig. 8E) as well as *Staphylococcus aureus* that can cause bacteremia,
346 skin infection, respiratory infections and food poisoning (Fig. 8F). The last three bacterial
347 pathogens were in sputum samples and imaged using the *high mag imaging module* with a
348 100x/1.25 oil immersion objective. In the last sample, since the bacteria are distributed in
349 different z-plane, a z-stack was taken to capture all within the field of view.

350 Discussion

351 Here we report the concept and implementation of a modular and automated imaging plat-
352 form. Compared to directly modifying existing microscopes [56] and many other monolithic
353 designs, the open nature of our platform and its high degree of modularity offers flexibility
354 and greatly simplifies both iterative and derivative developments, making it easy to adapt
355 the tool to specific applications. CNC machining also allows the precision and robustness
356 unmatched by 3D-printing. While we demonstrated bright field, dark field and fluores-
357 cent imaging with reversed lens configuration and using standard objectives, other imaging
358 modalities such as Fourier Ptychography [15, 57], holography/lensless imaging [16, 58] as
359 well as standard or LED-matrix and computation-based phase contrast [59, 60] can also be
360 implemented on our platform. Furthermore, metalens made of a single layer of nanostruc-
361 tures [61] may be adopted in place of standard objectives as they become available. The
362 compactness and light weight makes it possible to mount the lens on a voice coil actuator
363 (widely used in cellphone cameras and blu-ray players), eliminating the need for linear stage,
364 which results in reduction in cost and form factor. Metasurfaces or phase masks may also
365 be incorporated into the optical train for aberration correction [62] and for enhanced 3D
366 imaging capability through point spread function engineering [63, 64, 65]. While all images

367 in this report are taken with Pi cameras, CMOS cameras that are low-cost and compact but
368 rival the performance of sCMOS and EMCCD can be used for more demanding applications
369 [66, 67, 68, 69]. With modular design, other XY stage designs may also be used to allow
370 larger travel and/or more precise motion [70, 13, 71].

371 Applying the imaging platform to the diagnosis of malaria, we developed a new solution
372 that can determine parasitemia with high degree of automation and very high throughput.
373 While there are five strains of parasites that can cause malaria in human, in this study we
374 focused on Plasmodium falciparum (*P. falciparum*) for two reasons. First, *P. falciparum* is
375 the deadliest strain, which can cause fatality if treatment is delayed beyond 24 hours after
376 the onset of clinical symptoms. *P. falciparum* has also developed resistance to nearly all
377 anti-malarials in current use, where chloroquine-resistance has spread to nearly all areas
378 of the world where *P. falciparum* malaria is transmitted [72]. Second, in 2017, the WHO
379 African Region was home to 92% of global malaria cases, out of which 99.7% of is due
380 to *P. falciparum* [73]. The dominance of *P. falciparum* in this region makes our low-mag
381 module-based solution readily applicable without considering the need for speciation. While
382 at low magnification morphology of ring stage parasites cannot be resolved, in the future,
383 other features may be used for speciation. For example, in contrast to *P. falciparum* where
384 most parasites present in the peripheral blood are in ring-stage due to sequestration, both
385 trophozoites and schizonts can be present for *P. vivax* (Pv). Compared to ring stage, these
386 stages have markedly different morphology features that are likely resolvable even with low
387 magnification [74] and should present more intense and more red-shifted fluorescence.

388 We have also demonstrated that morphological features of ring-stage parasites can be
389 unambiguously resolved with the *high mag imaging module* on the platform. The *high mag*
390 *imaging module* may be combined with the *low mag imaging module* for further improved
391 detection limit and speciation capability without sacrificing throughput. To do so, the slide
392 is first screened by the *low mag imaging module*, where locations of suspected pathogens are
393 recorded. The spots are then relocated with the motorized scanner and imaged with the *high*

394 *mag imaging module* for confirmation. The platform may also be modified to accommodate
395 two imaging modules simultaneously. Encouraged by presented results, we are in planning
396 phase of a clinical trial for testing the efficacy of the instrument in field conditions in both
397 India and Africa.

398 We have shown that using a color CMOS sensor and long pass emission filter for fluo-
399 rescence imaging, spectral shift of DAPI-stained *P. falciparum* parasites on the order of 10
400 nm can be reliably detected in a single shot. This proved to be critical in the application
401 of diagnosis of malaria using blood smears. The loss in spatial resolution compared to us-
402 ing a monochrome sensor under the same condition may be complemented by using higher
403 magnification (without changing the NA of the objective). When the fluorescent spots arise
404 from diffraction limited sources or beads of known size and some emission spectrum infor-
405 mation is known a priori, maximum likelihood estimation may be used to optimally extract
406 information. This spectral imaging capability allows single-shot multiplexed detection with
407 a single laser excitation.

408 While we used nucleic acid stains for sensitive detection of *P. falciparum* parasites in thin
409 blood smear, different probes that are specific to a set of pathogens can also be utilized. The
410 past decades has seen much development of pathogen specific probes [75, 76, 77, 78]. Being
411 low-cost and highly configurable, *Octopi* has the potential to help realize the wide spread use
412 of these new probes in field diagnostics. Besides diagnosis of disease in field conditions, the
413 automated imaging platform can be also be adapted for research applications. In particular,
414 because of its low cost and small footprint, many units can be set up in a single lab to
415 parallelize experiments like super-resolution microscopy [79, 80], expansion microscopy [81],
416 spatially resolved profiling of RNA in single cells [82] and spatial sequencing of single-cell
417 transcriptional states in tissues[83].

418 With the emergence of deep learning in microscopy, the capabilities of *Octopi* can be
419 boosted by newly developed neural networks that breaks the limits of what is possible in
420 traditional microscopy [84, 85, 86, 87, 88, 84, 89, 90]. As a highly scalable platform, *Octopi*

421 can also help bring training and deployment of these networks to a large number of users.
422 Finally, with a large network of *Octopi* deployed around the world, we envision to bring
423 together researchers, developers and clinical practitioners to collectively advance microscopy-
424 based disease diagnostics.

425 **Materials and Methods**

426 **Study Design**

427 The goal of this study is to develop and evaluate a low-cost, modular and automated mi-
428 croscope platform for a range of applications including, in particular, diagnosis of infectious
429 disease with high throughput in resource-limited settings. We started by implementing
430 modules of the microscope and characterizing their performances, showing that performance
431 comparable to high end research grade microscope can be achieved. In applying the platform
432 to detection of ring-stage *P. falciparum* parasites, we discovered that with 405 nm laser exci-
433 tation, a 435 nm long pass emission filter and a color CMOS camera, DAPI-stained parasites
434 and platelets may be told apart by color. We used laser scanning confocal microscopy to
435 obtain spectrum of emitted fluorescence from DAPI stained platelets and parasites in pa-
436 tient sample, which revealed a spectral red-shift on the order of 10 nm. That this shift and
437 the resulting color difference can be used to differentiate parasites and platelets under low
438 magnification was supported by simulation. To automatically detect parasites and quantify
439 diagnostic performance that may be achieved, we collected data from 8 smears of *P. falci-*
440 *parum* culture and 10 smears of uninfected blood and trained a classifier using these data.
441 This amounts to baseline data on 109,3555 spots of parasites (*P. falciparum*) and 437,944
442 spots for uninfected whole blood. Based on this classifier we simulated sensitivity and speci-
443 ficity that can be expected at different parasitemia. A processing pipeline was implemented
444 on Jetson Nano so that computation can be performed locally in real time. Furthermore,
445 we imaged lab and patient samples on our platform with high magnification to show that

446 morphology of ring-stage parasites can also be resolved, implying further improved sensitiv-
447 ity and specificity can be achieved. Finally, to show broad applicability of our platform, we
448 imaged different prepared pathological samples with different magnifications.

449 **Construction of the prototype microscope**

450 Custom parts of the microscope were designed with Autodesk Inventor Professional and
451 fabricated by Protolabs and 3D Hubs (CNC machining with 6061 Aluminum), and Fictiv
452 (selective laser sintering with Nylon) (Fig. S9). In the *high mag imaging module*, a piezo
453 stack actuator with end cap (Thorlabs PK2FMP2) was epoxied to the extended contact
454 ball bearing linear stage (SELN LBV40-C2). A 12-bit DAC (Adafruit MCP4725 breakout
455 board) was interfaced with the Raspberry Pi computer through I2C interface. The output
456 of the DAC was amplified by a miniature piezo driver (PiezoDrive PDu100B) to drive the
457 piezo stack actuator. Three stepper motor driver boards (Allegro A3967-based Easydriver)
458 were used to drive the lead screw linear motors and captive linear actuator (Haydon Kerk
459 Pittman 21H4AC-2.5-907).

460 **Scanning stage flatness characterization**

461 A LabView program was developed to raster scan a target slide (Ossila S151 Ultra-flat
462 Quartz Coated Glass) while recording the relative z-position of top surface of the slide at
463 the center of the microscope field of view, which is measured by a non-contact displacement
464 sensor (MKS Instrument Optimet ConoPoint-3R, Fig. S2). The measurement results were
465 saved as CSV files and processed with MATLAB.

466 **Deep learning-based red blood cell segmentation**

467 The 91-layer Fully Convolutional DenseNet contains 11 dense blocks (with 4, 5, 7, 10, 12,
468 15, 12, 10, 7, 5 and 4 layers for each block), and was trained from scratch. Weights of

469 the convolutional layers were initialized using He initialization [91]. For training, Adam
470 optimizer [92] was used with a learning rate of 0.001 and batch size of 16.

471 To deal with the more frequent false negatives (RBC pixels labeled as non-RBC pixels)
472 compared to false positives (non-RBC pixels as RBC pixels) in the labels of the training data,
473 class weights were introduced in the binary cross-entropy loss function. Specifically, false
474 negatives was associated with a class weight of 10, whereas false positives were associated
475 with a class weight of 0.1. This ensured that mispredictions made on pixels labeled positive,
476 where labels are reliable, are penalized more heavily than mispredictions made on pixels
477 labeled negative, where labels can be noisy.

478 To obtain a large labeled training data set without tedious human annotation, the fol-
479 lowing two-step approach is taken. First, Hough transform was used to generate accurate
480 segmentation masks for images where red blood cells are round and isolated. Second, mul-
481 tiple such images were superimposed and distorted through shear transformations to mimic
482 images with red blood cells that are not round and/or overlapping. The resulting images,
483 which also have accurate masks, were used to augment the training data. In total, 22,680
484 images of size 128×128 were used for training the neural network.

485 The benefits of using data augmentation and introduction of class weights are visualized
486 in Fig. S10.

487 **Spot detection from fluorescent images obtained with the *low mag*** 488 ***imaging module***

489 Two spot detection pipeline were implemented. The CPU-only pipeline (pipeline A) was
490 implemented in python with the scikit-image package. The pipeline that takes advantage
491 of CUDA (pipeline B) was implemented in C++ with the OpenCV library and python
492 with the scikit-image package. Both pipelines take an image of size $1428 \times 1428 \times 3$ as in-
493 put and convert it to grayscale for further processing. In pipeline A, functions `skim-`
494 `age.morphology.white_tophat` and `skimage.feature.blob_log` are used. In pipeline B, image

495 is uploaded to GPU and background removed using tophat filtering with disk diameter of 9.
496 The processed image remains in GPU and is converted from CV_U8 to CV_F32. Four nor-
497 malized Laplacian of Gaussian images (LoG1,LoG2,LoG3,LoG4) with gaussian sigam equal
498 to 1, 1.5, 2 and 2.5 are computed by applications of a Gaussian filter followed by a Lapla-
499 cian filter and scale normalization. The four images are compared with a manually selected
500 threshold, and pixel whose value is smaller than the threshold is set to zero. A maximum
501 projection along the scale dimension of the four LoG images is computed and and a 3x3
502 maximum filter is applied. The resulting image (P) is compared with the four LoG images,
503 and locations where pixel values equal are recorded in a mask M initialized with zeros (for
504 example, if $\text{LoG3}(r,c)=P(r,c)$, then $M(r,c)$ is set to 3). The mask, which stores locations
505 of 3x3x4 local maximums, is downloaded from GPU, and 3D coordinates (2D location +
506 scale) of non-zero elements of the mask are exported as a three column array. The array
507 is loaded in python for removal of spots with overlap exceeding the a set threshold of 0.5.
508 The last step takes advantage of the already implemented `skimage.feature.blob._prune_blobs`
509 function, which uses a KDtree implemented in c to perform nearest neighbour search for
510 significantly reducing the number of pairwise comparison needed.

511 Before passing to the spot detection processing pipeline, fluorescent images were first
512 converted from sRGB space to linear RGB space, so that pixel intensity has a linear rela-
513 tionship to the number of photons collected. Detected spots were saved for visualization and
514 downstream classification.

515 **Fluorescent spot classifier**

516 The gradient boosted decision trees classifier was implemented using `XGBClassifier` from the
517 `xgboost` python package. Features for each fluorescent spot passed as input to the classifier
518 and their relevance are shown in Fig. S11. Among the features, overlap is the sum of pixel
519 values of pixels that are segmented as part of red blood cells over the sum of pixel values of
520 all pixel. For uninfected whole blood, this feature is directly computed from data. For *P*.

521 *falciparum* culture, because the red blood cells are ill-shaped for bright field segmentation,
522 this feature was sampled from a empirical distribution, as is plotted in Fig. S12. Performance
523 of the classifier was measured using 20-fold cross validation. Each each fold is made of 3
524 smears of uninfected whole blood slides and 3 smears of *P. falciparum* lab culture, picked
525 at random. For training the classifier, binary logistic loss function was used with a L2
526 regularization term.

527 **Image processing**

528 For all the images presented, image processing were done in MATLAB. For brightfield images,
529 illumination correction is done through normalization against a blank image (image of a blank
530 slide). For fluorescent images, background removal is done through tophat transform. Bright
531 field images from both the *low mag imaging module* and the *high mag imaging module* and
532 fluorescent images from the *high mag imaging module* are demosaiced in MATLAB from the
533 raw bayer data. For images that are denoised (as noted in figure captions), denoising is done
534 using a convolutional neural network FFDNet [93]. Comparisons of images before and after
535 denoising can be found in Fig. S13.

536 **P. falciparum in vitro cultures**

537 Plasmodium Falciparum culture were provided by the Yeh lab at Stanford University where
538 Plasmodium falciparum W2 (MRA-157) were obtained from MR4. Parasites were grown in
539 human erythrocytes (2% hematocrit, obtained from the Stanford Blood Center) in RPMI
540 1640 media supplemented with 0.25% Albumax II (GIBCO Life Technologies), 2 g/L sodium
541 bicarbonate, 0.1 mM hypoxanthine, 25 mM HEPES (pH 7.4), and 50 g/L gentamycin, at
542 37C, 5% O2, and 5% CO2.

543 **Blood Sample from healthy donors and from patients diagnosed** 544 **with malaria**

545 De-identified blood sample (whole blood) from healthy anonymous donors were obtained
546 from the Stanford Blood Center in BD Vacutainer blood collection tubes. De-identified
547 methanol-fixed finger prick blood smears from patients diagnosed with malaria were provided
548 by UCSF Malaria Elimination Initiative (MEI)/Infectious Disease Research Collaboration,
549 Kampala, Uganda.

550 **Preparation and staining of blood smears**

551 Smears of blood from healthy donors and *P. falciparum* culture were fixed by dipping in
552 absolute methanol for 30 seconds. Fixed smears were incubated with 5 $\mu\text{g}/\text{ml}$ DAPI solution
553 for 1 minute, washed in water, and let air dry in the dark. DAPI solution was purchased
554 from Biotium (catalog # 40043) and diluted. Samples were kept in dark before imaging.

555 **Other pathology samples**

556 Prepared slides of *Loa-Loa*, *Leishmania donovani*, *Mycobacterium tuberculosis* were acquired
557 from VWR (catalog Number 470182-158, 470181-894, 470177-208 respectively). Prepared
558 slide of Schistosomiasis of Intestines was acquired from AmScope (SKU: PS50HP). Pre-
559 pared slide of *Trypanosoma brucei rhodesiense* was acquired from Carolina (item # 295822).
560 Prepared slides of *Streptococcus pneumoniae* and *Staphylococcus aureus* in sputum were de-
561 identified and provided by the Clinical Microbiology Laboratory at Stanford Health Care.

562 **Statistical Analysis**

563 Simulation of per case sensitivity and specificity (Fig. 6E) was done in MATLAB. For each
564 parasitemia and per spot false positive rate (FPR) (and its associated per spot false negative
565 rate FNR), 10,000 tests were simulated. In each test, the total number of platelets (N) and

566 parasites (P) was sampled from Poisson distributions; the number of detected parasites was
567 the sum of true positives and false positives, both sampled from Bernoulli distribution, with
568 parameters ($P, 1\text{-FNR}$) and (N, FPR).

569 References

- 570 [1] E. Yusuf and R. L. Hamers, “What the WHO’s List of Essential Diagnostics means for
571 clinical microbiology laboratories and antimicrobial stewardship practice worldwide,”
572 *Clinical Microbiology and Infection*, vol. 25, pp. 6–9, jan 2019.
- 573 [2] E. Fu, P. Yager, P. N. Floriano, N. Christodoulides, and J. T. McDevitt, “Perspective
574 on diagnostics for global health,” *IEEE Pulse*, vol. 2, no. 6, pp. 40–50, 2011.
- 575 [3] K. J. Land, D. I. Boeras, X.-S. Chen, A. R. Ramsay, and R. W. Peeling, “Reassured
576 diagnostics to inform disease control strategies, strengthen health systems and improve
577 patient outcomes,” *Nature microbiology*, vol. 4, no. 1, p. 46, 2019.
- 578 [4] D. Berger, “A brief history of medical diagnosis and the birth of the clinical laboratory.
579 Part 1–Ancient times through the 19th century.,” *MLO: medical laboratory observer*,
580 vol. 31, pp. 28–30, 32, 34–40, jul 1999.
- 581 [5] B. A. Mathison and B. S. Pritt, “Update on Malaria Diagnostics and Test Utilization,”
582 *Journal of Clinical Microbiology*, vol. 55, no. 7, pp. 2009–2017, 2017.
- 583 [6] WHO, “Malaria microscopy quality assurance manual Ver. 2,” tech. rep., 2016.
- 584 [7] N. Farahani and C. E. Monteith, “The coming paradigm shift: A transition from manual
585 to automated microscopy,” *Journal of pathology informatics*, vol. 7, p. 35, sep 2016.
- 586 [8] A. F. Coskun, S. N. Topkaya, A. K. Yetisen, and A. E. Cetin, “Portable multiplex
587 optical assays,” *Advanced Optical Materials*, vol. 7, no. 4, p. 1801109, 2019.

- 588 [9] Q. Wei, H. Qi, W. Luo, D. Tseng, S. J. Ki, Z. Wan, Z. Gracs, L. A. Bentolila, T.-T.
589 Wu, R. Sun, *et al.*, “Fluorescent imaging of single nanoparticles and viruses on a smart
590 phone,” *ACS nano*, vol. 7, no. 10, pp. 9147–9155, 2013.
- 591 [10] J. S. Cybulski, J. Clements, and M. Prakash, “Foldscope: origami-based paper micro-
592 scope,” *PloS one*, vol. 9, no. 6, p. e98781, 2014.
- 593 [11] A. Skandarajah, C. D. Reber, N. A. Switz, and D. A. Fletcher, “Quantitative imaging
594 with a mobile phone microscope,” *PloS one*, vol. 9, no. 5, p. e96906, 2014.
- 595 [12] M. V. D’Ambrosio, M. Bakalar, S. Bennuru, C. Reber, A. Skandarajah, L. Nilsson,
596 N. Switz, J. Kamgno, S. Pion, M. Boussinesq, *et al.*, “Point-of-care quantification of
597 blood-borne filarial parasites with a mobile phone microscope,” *Science translational*
598 *medicine*, vol. 7, no. 286, pp. 286re4–286re4, 2015.
- 599 [13] J. P. Sharkey, D. C. Foo, A. Kabla, J. J. Baumberg, and R. W. Bowman, “A one-piece
600 3d printed flexure translation stage for open-source microscopy,” *Review of Scientific*
601 *Instruments*, vol. 87, no. 2, p. 025104, 2016.
- 602 [14] O. Holmström, N. Linder, B. Ngasala, A. Mårtensson, E. Linder, M. Lundin, H. Moila-
603 nen, A. Suutala, V. Diwan, and J. Lundin, “Point-of-care mobile digital microscopy and
604 deep learning for the detection of soil-transmitted helminths and schistosoma haemato-
605 bium,” *Global health action*, vol. 10, no. sup3, p. 1337325, 2017.
- 606 [15] G. Zheng, R. Horstmeyer, and C. Yang, “Wide-field, high-resolution Fourier ptycho-
607 graphic microscopy,” *Nature Photonics*, vol. 7, no. 9, pp. 739–745, 2013.
- 608 [16] A. Greenbaum, Y. Zhang, A. Feizi, P.-L. Chung, W. Luo, S. R. Kandukuri, and A. Oz-
609 can, “Wide-field computational imaging of pathology slides using lens-free on-chip mi-
610 croscopy,” *Science translational medicine*, vol. 6, no. 267, pp. 267ra175–267ra175, 2014.

- 611 [17] A. Ozcan and E. McLeod, “Lensless imaging and sensing,” *Annual review of biomedical*
612 *engineering*, vol. 18, pp. 77–102, 2016.
- 613 [18] Y. Wu and A. Ozcan, “Lensless digital holographic microscopy and its applications in
614 biomedicine and environmental monitoring,” *Methods*, vol. 136, pp. 4–16, 2018.
- 615 [19] A. Ozcan, “Mobile phones democratize and cultivate next-generation imaging, diagnos-
616 tics and measurement tools,” *Lab on a Chip*, vol. 14, no. 17, pp. 3187–3194, 2014.
- 617 [20] I. Hernández-Neuta, F. Neumann, J. Brightmeyer, T. Ba Tis, N. Madaboosi, Q. Wei,
618 A. Ozcan, and M. Nilsson, “Smartphone-based clinical diagnostics: towards democra-
619 tization of evidence-based health care,” *Journal of internal medicine*, vol. 285, no. 1,
620 pp. 19–39, 2019.
- 621 [21] WHO, “World Malaria Report. 2018. ISBN 978 92 4 156469 4.,” 2018.
- 622 [22] J. Daily, “Malaria diagnostics technology and market landscape,” 2016.
- 623 [23] U. Dalrymple, R. Arambepola, P. W. Gething, and E. Cameron, “How long do rapid
624 diagnostic tests remain positive after anti-malarial treatment?,” *Malaria journal*, vol. 17,
625 no. 1, p. 228, 2018.
- 626 [24] D. Gamboa, M.-F. Ho, J. Bendezu, K. Torres, P. L. Chiodini, J. W. Barnwell, S. In-
627 cardona, M. Perkins, D. Bell, J. McCarthy, *et al.*, “A large proportion of *p. falciparum*
628 isolates in the amazon region of peru lack *pfhrp2* and *pfhrp3*: implications for malaria
629 rapid diagnostic tests,” *PloS one*, vol. 5, no. 1, p. e8091, 2010.
- 630 [25] W. H. Organization *et al.*, “False-negative rdt results and implications of new reports
631 of *p. falciparum* histidine-rich protein 2/3 gene deletions,” tech. rep., World Health
632 Organization, 2017.
- 633 [26] C. L. Cohen, Y. Eshel, J. Swaminathan, D. Gluck, D. Maina, C. Mbithi, S. On-
634 songo, Z. Premji, N. Lezmy, Z. Nneka, S. Levy-Schreier, J. J. Pollak, S. J. Salpeter,

- 635 H. Benkuzari, H. Solomon, M. Charles, P. Sampathkumar, M. Soni, and A. Hourii-
636 Yafin, “Evaluation of the Parasight Platform for Malaria Diagnosis,” *Journal of Clinical*
637 *Microbiology*, vol. 55, no. 3, pp. 768–775, 2017.
- 638 [27] C. B. Delahunt, C. Mehanian, L. Hu, S. K. McGuire, C. R. Champlin, M. P. Horning,
639 B. K. Wilson, and C. M. Thompon, “Automated microscopy and machine learning for
640 expert-level malaria field diagnosis,” in *2015 IEEE Global Humanitarian Technology*
641 *Conference (GHTC)*, pp. 393–399, IEEE, 2015.
- 642 [28] A. Maxmen, “How to defuse malaria’s ticking time bomb,” *Nature*, vol. 559, pp. 458–
643 465, 2018.
- 644 [29] K. Haldar, S. Bhattacharjee, and I. Safeukui, “Drug resistance in Plasmodium,” *Nature*
645 *Reviews Microbiology*, vol. 16, no. 3, pp. 156–170, 2018.
- 646 [30] A. J. Abdifatah, C. Wanna, and N.-B. Kesara, “Plasmodium falciparum drug resistance
647 gene status in the Horn of Africa: A systematic review,” *African Journal of Pharmacy*
648 *and Pharmacology*, vol. 12, no. 25, pp. 361–373, 2018.
- 649 [31] WHO, “Status report on artemisinin resistance and ACT efficacy (August 2018),”
650 no. August, 2018.
- 651 [32] W. H. Organization, *Malaria Microscopy Quality Assurance Manual-Version 2*. World
652 Health Organization, 2016.
- 653 [33] N. A. Switz, M. V. D’Ambrosio, and D. A. Fletcher, “Low-cost mobile phone microscopy
654 with a reversed mobile phone camera lens,” *PloS one*, vol. 9, no. 5, p. e95330, 2014.
- 655 [34] S. Jiang, Z. Bian, X. Huang, P. Song, H. Zhang, Y. Zhang, and G. Zheng, “Rapid
656 and robust whole slide imaging based on led-array illumination and color-multiplexed
657 single-shot autofocusing,” *arXiv preprint arXiv:1905.03371*, 2019.

- 658 [35] H. Pinkard, Z. Phillips, A. Babakhani, D. A. Fletcher, and L. Waller, “Deep learning
659 for single-shot autofocus microscopy,” *Optica*, vol. 6, no. 6, pp. 794–797, 2019.
- 660 [36] J. Sun, C. Zuo, J. Zhang, Y. Fan, and Q. Chen, “High-speed Fourier ptychographic
661 microscopy based on programmable annular illuminations,” *Scientific Reports*, vol. 8,
662 no. 1, pp. 1–12, 2018.
- 663 [37] A. GmbH, “Dapi, product no. a1001,”
- 664 [38] F. Otto, “Dapi staining of fixed cells for high-resolution flow cytometry of nuclear dna,”
665 in *Methods in cell biology*, vol. 33, pp. 105–110, Elsevier, 1990.
- 666 [39] T. Lindeberg, “Scale-space theory: A basic tool for analyzing structures at different
667 scales,” *Journal of applied statistics*, vol. 21, no. 1-2, pp. 225–270, 1994.
- 668 [40] T. Lindeberg, “Feature detection with automatic scale selection,” *International journal
669 of computer vision*, vol. 30, no. 2, pp. 79–116, 1998.
- 670 [41] S. Jégou, M. Drozdal, D. Vazquez, A. Romero, and Y. Bengio, “The one hundred layers
671 tiramisu: Fully convolutional densenets for semantic segmentation,” in *Proceedings of
672 the IEEE Conference on Computer Vision and Pattern Recognition Workshops*, pp. 11–
673 19, 2017.
- 674 [42] S. Han, H. Mao, and W. J. Dally, “Deep compression: Compressing deep neural
675 networks with pruning, trained quantization and huffman coding,” *arXiv preprint
676 arXiv:1510.00149*, 2015.
- 677 [43] L.-C. Chen, Y. Zhu, G. Papandreou, F. Schroff, and H. Adam, “Encoder-decoder with
678 atrous separable convolution for semantic image segmentation,” in *ECCV*, 2018.
- 679 [44] M. Sandler, A. Howard, M. Zhu, A. Zhmoginov, and L.-C. Chen, “Mobilenetv2: Inverted
680 residuals and linear bottlenecks,” in *CVPR*, 2018.

- 681 [45] B. Sun, L. Yang, P. Dong, W. Zhang, J. Dong, and C. Young, “Ultra power-efficient
682 cnn domain specific accelerator with 9.3tops/watt for mobile and embedded applica-
683 tions,” in *The IEEE Conference on Computer Vision and Pattern Recognition (CVPR)*
684 *Workshops*, June 2018.
- 685 [46] F. Kawamoto, “Rapid diagnosis of malaria by fluorescence microscopy with light mi-
686 croscope and interference filter,” *The Lancet*, vol. 337, no. 8735, pp. 200–202, 1991.
- 687 [47] R. Guy, P. Liu, P. Pennefather, and I. Crandall, “The use of fluorescence enhancement
688 to improve the microscopic diagnosis of falciparum malaria,” *Malaria journal*, vol. 6,
689 no. 1, p. 89, 2007.
- 690 [48] M. P. Horning, C. B. Delahunt, S. R. Singh, S. H. Garing, and K. P. Nichols, “A paper
691 microfluidic cartridge for automated staining of malaria parasites with an optically
692 transparent microscopy window,” *Lab on a chip*, vol. 14, no. 12, pp. 2040–2046, 2014.
- 693 [49] J. Kapuscinski, “Interactions of nucleic acids with fluorescent dyes: spectral properties
694 of condensed complexes,” *Journal of Histochemistry & Cytochemistry*, vol. 38, no. 9,
695 pp. 1323–1329, 1990.
- 696 [50] S. H. Apte, P. L. Groves, J. S. Roddick, V. P. da Hora, and D. L. Doolan,
697 “High-throughput multi-parameter flow-cytometric analysis from micro-quantities of
698 plasmodium-infected blood,” *International journal for parasitology*, vol. 41, no. 12,
699 pp. 1285–1294, 2011.
- 700 [51] S. Cervantes, J. Prudhomme, D. Carter, K. G. Gopi, Q. Li, Y.-T. Chang, and K. G.
701 Le Roch, “High-content live cell imaging with rna probes: advancements in high-
702 throughput antimalarial drug discovery,” *BMC cell biology*, vol. 10, no. 1, p. 45, 2009.
- 703 [52] N. Regev-Rudzki, D. W. Wilson, T. G. Carvalho, X. Sisquella, B. M. Coleman, M. Rug,
704 D. Bursac, F. Angrisano, M. Gee, A. F. Hill, *et al.*, “Cell-cell communication between

- 705 malaria-infected red blood cells via exosome-like vesicles,” *Cell*, vol. 153, no. 5, pp. 1120–
706 1133, 2013.
- 707 [53] X. Sisquella, Y. Ofir-Birin, M. A. Pimentel, L. Cheng, P. A. Karam, N. G. Sampaio,
708 J. S. Penington, D. Connolly, T. Giladi, B. J. Scicluna, *et al.*, “Malaria parasite dna-
709 harbouring vesicles activate cytosolic immune sensors,” *Nature communications*, vol. 8,
710 no. 1, p. 1985, 2017.
- 711 [54] K. A. Babatunde, S. Mbagwu, M. A. Hernández-Castañeda, S. R. Adapa, M. Walch,
712 L. Filgueira, L. Falquet, R. H. Jiang, I. Ghiran, and P.-Y. Mantel, “Malaria infected
713 red blood cells release small regulatory rnas through extracellular vesicles,” *Scientific*
714 *reports*, vol. 8, no. 1, p. 884, 2018.
- 715 [55] Y. Ofir-Birin, P. Abou Karam, A. Rudik, T. Giladi, Z. Porat, and N. Regev-Rudzki,
716 “Monitoring extracellular vesicle cargo active uptake by imaging flow cytometry,” *Frontiers in immunology*,
717 vol. 9, p. 1011, 2018.
- 718 [56] Z. Bian, G. Zheng, K. Guo, X. Heng, and J. Liao, “InstantScope: a low-cost whole slide
719 imaging system with instant focal plane detection,” *Biomedical Optics Express*, vol. 6,
720 no. 9, p. 3210, 2015.
- 721 [57] T. Aidukas, R. Eckert, A. R. Harvey, L. Waller, and P. C. Konda, “Low-cost, sub-micron
722 resolution, wide-field computational microscopy using opensource hardware,” *Scientific*
723 *reports*, vol. 9, no. 1, p. 7457, 2019.
- 724 [58] N. Antipa, G. Kuo, R. Heckel, B. Mildenhall, E. Bostan, R. Ng, and L. Waller, “Dif-
725 fusercam: lensless single-exposure 3d imaging,” *Optica*, vol. 5, no. 1, pp. 1–9, 2018.
- 726 [59] L. Tian, J. Wang, and L. Waller, “3d differential phase-contrast microscopy with com-
727 putational illumination using an led array,” *Optics letters*, vol. 39, no. 5, pp. 1326–1329,
728 2014.

- 729 [60] L. Tian and L. Waller, “Quantitative differential phase contrast imaging in an led array
730 microscope,” *Optics express*, vol. 23, no. 9, pp. 11394–11403, 2015.
- 731 [61] M. Khorasaninejad, W. T. Chen, R. C. Devlin, J. Oh, A. Y. Zhu, and F. Capasso,
732 “Metalenses at visible wavelengths: Diffraction-limited focusing and subwavelength res-
733 olution imaging,” *Science*, vol. 352, no. 6290, pp. 1190–1194, 2016.
- 734 [62] W. T. Chen, A. Y. Zhu, J. Sisler, Y.-W. Huang, K. M. Yousef, E. Lee, C.-W. Qiu,
735 and F. Capasso, “Broadband achromatic metasurface-refractive optics,” *Nano letters*,
736 vol. 18, no. 12, pp. 7801–7808, 2018.
- 737 [63] S. R. P. Pavani, M. A. Thompson, J. S. Biteen, S. J. Lord, N. Liu, R. J. Twieg,
738 R. Piestun, and W. Moerner, “Three-dimensional, single-molecule fluorescence imaging
739 beyond the diffraction limit by using a double-helix point spread function,” *Proceedings*
740 *of the National Academy of Sciences*, vol. 106, no. 9, pp. 2995–2999, 2009.
- 741 [64] Y. Shechtman, S. J. Sahl, A. S. Backer, and W. Moerner, “Optimal point spread function
742 design for 3d imaging,” *Physical review letters*, vol. 113, no. 13, p. 133902, 2014.
- 743 [65] A. S. Backer and W. Moerner, “Extending single-molecule microscopy using optical
744 fourier processing,” *The Journal of Physical Chemistry B*, vol. 118, no. 28, pp. 8313–
745 8329, 2014.
- 746 [66] H. Ma, R. Fu, J. Xu, and Y. Liu, “A simple and cost-effective setup for super-resolution
747 localization microscopy,” *Scientific reports*, vol. 7, no. 1, p. 1542, 2017.
- 748 [67] R. Diekmann, K. Till, M. Müller, M. Simonis, M. Schüttpelz, and T. Huser, “Charac-
749 terization of an industry-grade cmos camera well suited for single molecule localization
750 microscopy—high performance super-resolution at low cost,” *Scientific reports*, vol. 7,
751 no. 1, p. 14425, 2017.

- 752 [68] H. P. Babcock, “Multiplane and spectrally-resolved single molecule localization mi-
753 croscopy with industrial grade cmos cameras,” *Scientific reports*, vol. 8, no. 1, p. 1726,
754 2018.
- 755 [69] B. Diederich, P. Then, A. Jügler, R. Förster, and R. Heintzmann, “cellstormcost-
756 effective super-resolution on a cellphone using dstorm,” *PloS one*, vol. 14, no. 1,
757 p. e0209827, 2019.
- 758 [70] R. A. Campbell, R. W. Eifert, and G. C. Turner, “Openstage: a low-cost motorized mi-
759 croscope stage with sub-micron positioning accuracy,” *PloS one*, vol. 9, no. 2, p. e88977,
760 2014.
- 761 [71] D. Schneidereit, L. Kraus, J. C. Meier, O. Friedrich, and D. F. Gilbert, “Step-by-step
762 guide to building an inexpensive 3d printed motorized positioning stage for automated
763 high-content screening microscopy,” *Biosensors and Bioelectronics*, vol. 92, pp. 472–481,
764 2017.
- 765 [72] P. B. Bloland, W. H. Organization, *et al.*, “Drug resistance in malaria,” tech. rep.,
766 Geneva: World Health Organization, 2001.
- 767 [73] W. H. Organization, *World malaria report 2018*. World Health Organization, 2019.
- 768 [74] W. H. Organization and C. for Disease Control, *Basic malaria microscopy*. World Health
769 Organization, 2010.
- 770 [75] E. F. DeLong, G. S. Wickham, and N. R. Pace, “Phylogenetic stains: ribosomal rna-
771 based probes for the identification of single cells,” *Science*, vol. 243, no. 4896, pp. 1360–
772 1363, 1989.
- 773 [76] J. Shah, O. Mark, H. Weltman, N. Barcelo, W. Lo, D. Wronska, S. Kakkilaya, A. Rao,
774 S. T. Bhat, R. Sinha, *et al.*, “Fluorescence in situ hybridization (fish) assays for diag-
775 nosing malaria in endemic areas,” *PLoS One*, vol. 10, no. 9, p. e0136726, 2015.

- 776 [77] M. Kamariza, P. Shieh, C. S. Ealand, J. S. Peters, B. Chu, F. P. Rodriguez-Rivera,
777 M. R. B. Sait, W. V. Treuren, N. Martinson, R. Kalscheuer, *et al.*, “Rapid detection of
778 mycobacterium tuberculosis in sputum with a solvatochromic trehalose probe,” *Science*
779 *translational medicine*, vol. 10, no. 430, p. eaam6310, 2018.
- 780 [78] Y. Cheng, J. Xie, K.-H. Lee, R. L. Gaur, A. Song, T. Dai, H. Ren, J. Wu, Z. Sun,
781 N. Banaei, *et al.*, “Rapid and specific labeling of single live mycobacterium tuberculosis
782 with a dual-targeting fluorogenic probe,” *Science translational medicine*, vol. 10, no. 454,
783 p. eaar4470, 2018.
- 784 [79] E. Betzig, G. H. Patterson, R. Sougrat, O. W. Lindwasser, S. Olenych, J. S. Bonifacino,
785 M. W. Davidson, J. Lippincott-Schwartz, and H. F. Hess, “Imaging intracellular fluo-
786 rescent proteins at nanometer resolution,” *Science*, vol. 313, no. 5793, pp. 1642–1645,
787 2006.
- 788 [80] M. J. Rust, M. Bates, and X. Zhuang, “Sub-diffraction-limit imaging by stochastic
789 optical reconstruction microscopy (storm),” *Nature methods*, vol. 3, no. 10, p. 793,
790 2006.
- 791 [81] F. Chen, P. W. Tillberg, and E. S. Boyden, “Expansion microscopy,” *Science*, vol. 347,
792 no. 6221, pp. 543–548, 2015.
- 793 [82] K. H. Chen, A. N. Boettiger, J. R. Moffitt, S. Wang, and X. Zhuang, “Spatially resolved,
794 highly multiplexed rna profiling in single cells,” *Science*, vol. 348, no. 6233, p. aaa6090,
795 2015.
- 796 [83] X. Wang, W. E. Allen, M. A. Wright, E. L. Sylwestrak, N. Samusik, S. Vesuna, K. Evans,
797 C. Liu, C. Ramakrishnan, J. Liu, *et al.*, “Three-dimensional intact-tissue sequencing of
798 single-cell transcriptional states,” *Science*, vol. 361, no. 6400, p. eaat5691, 2018.

- 799 [84] M. Weigert, U. Schmidt, T. Boothe, A. Müller, A. Dibrov, A. Jain, B. Wilhelm,
800 D. Schmidt, C. Broaddus, S. Culley, *et al.*, “Content-aware image restoration: pushing
801 the limits of fluorescence microscopy,” *Nature methods*, vol. 15, no. 12, p. 1090, 2018.
- 802 [85] Y. Rivenson, Z. Göröcs, H. Günaydin, Y. Zhang, H. Wang, and A. Ozcan, “Deep
803 learning microscopy,” *Optica*, vol. 4, no. 11, pp. 1437–1443, 2017.
- 804 [86] Y. Rivenson and A. Ozcan, “Toward a thinking microscope: Deep learning in optical
805 microscopy and image reconstruction,” *arXiv preprint arXiv:1805.08970*, 2018.
- 806 [87] Y. Rivenson, H. Ceylan Koydemir, H. Wang, Z. Wei, Z. Ren, H. Günaydin, Y. Zhang,
807 Z. Gorocs, K. Liang, D. Tseng, *et al.*, “Deep learning enhanced mobile-phone mi-
808 croscopy,” *ACS Photonics*, vol. 5, no. 6, pp. 2354–2364, 2018.
- 809 [88] H. Wang, Y. Rivenson, Y. Jin, Z. Wei, R. Gao, H. Günaydin, L. A. Bentolila, C. Kural,
810 and A. Ozcan, “Deep learning enables cross-modality super-resolution in fluorescence
811 microscopy,” *Nat. Methods*, vol. 16, pp. 103–110, 2019.
- 812 [89] Y. Rivenson, T. Liu, Z. Wei, Y. Zhang, K. de Haan, and A. Ozcan, “Phasestain: the
813 digital staining of label-free quantitative phase microscopy images using deep learning,”
814 *Light: Science & Applications*, vol. 8, no. 1, p. 23, 2019.
- 815 [90] Y. Rivenson, H. Wang, Z. Wei, K. de Haan, Y. Zhang, Y. Wu, H. Günaydin, J. E.
816 Zuckerman, T. Chong, A. E. Sisk, *et al.*, “Virtual histological staining of unlabelled
817 tissue-autofluorescence images via deep learning,” *Nature Biomedical Engineering*, p. 1,
818 2019.
- 819 [91] K. He, X. Zhang, S. Ren, and J. Sun, “Delving deep into rectifiers: Surpassing human-
820 level performance on imagenet classification,” in *Proceedings of the IEEE international
821 conference on computer vision*, pp. 1026–1034, 2015.

822 [92] D. P. Kingma and J. Ba, “Adam: A method for stochastic optimization,” *arXiv preprint*
823 *arXiv:1412.6980*, 2014.

824 [93] K. Zhang, W. Zuo, and L. Zhang, “Ffdnet: Toward a fast and flexible solution for
825 cnn-based image denoising,” *IEEE Transactions on Image Processing*, vol. 27, no. 9,
826 pp. 4608–4622, 2018.

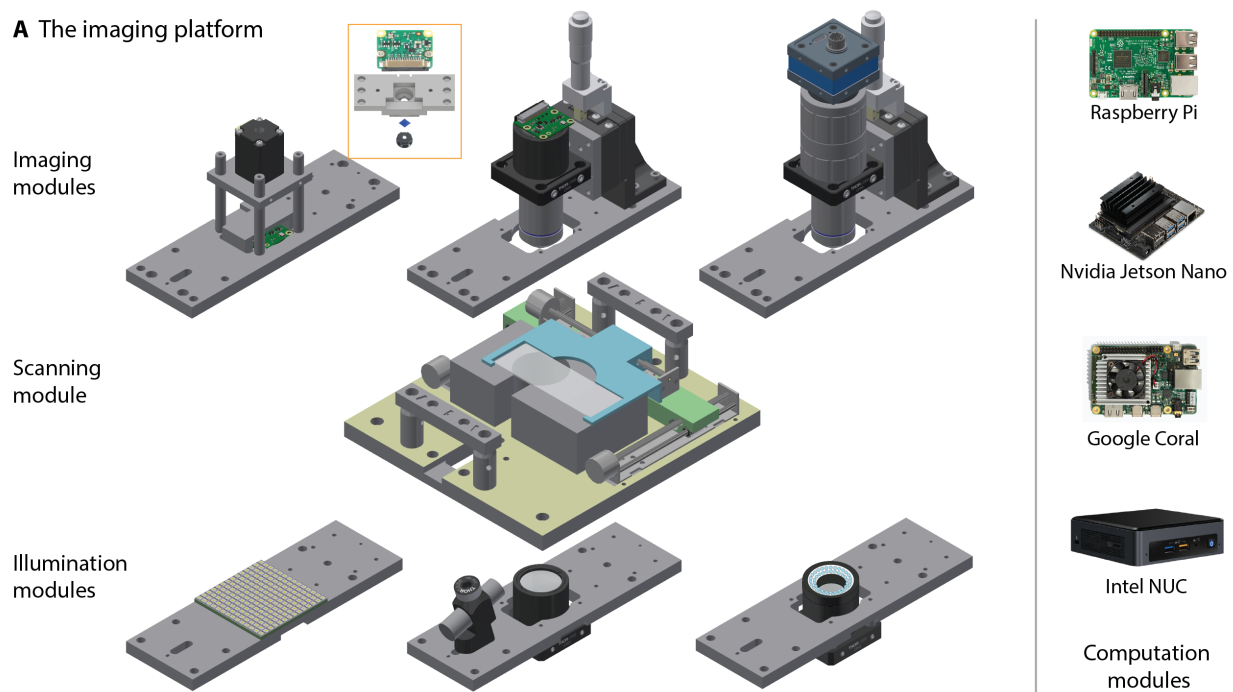
827 Acknowledgements

828 We acknowledge Ellen Yeh and her lab including Marta Walczak and Katrina Hong for pro-
829 viding *P. falciparum* blood cultures. We thank Grant Dorsey and Bryan Greenhouse from
830 UCSF and Harriet Ochokoru, laboratory technician at Infectious Diseases Research Collabo-
831 ration, Kampala, Uganda for providing de-identified patient blood smears via UCSF Malaria
832 Eliminate program. We thank Briec Cossic (Roche), Darvin Scott Smith (Stanford), Niaz
833 Banaei (Stanford) for providing non-malaria samples. We thank Andres Garchitorea and
834 Matt Bonds from PIVOT and Milijaona Randrianarivelosia from Institute Pasteur, Mada-
835 gascar and Sister Aquinas and staff of Swasthya Swaraj, Orissa, India and Vasundhara Ran-
836 gaswamy (Stanford) for fruitful discussions on diagnostics needs in Madagascar and India.
837 We thank MKS Instruments for providing ConoPoint-3 for stage flatness characterization.
838 Finally, we thank Mireille Kamariza (Stanford), Rishabh Manoj Shetty (Arizona State Uni-
839 versity) and all members of PrakashLab and specifically, Felix Hol, Haripriya Mukundara-
840 jan, Scott Coyle, Shailabh Kumar for feedback and comments on the manuscript. **Funding:**
841 H.L. was supported by a Bio-X Stanford Interdisciplinary Graduate Fellowship. L.F.V. was
842 supported by a Stanford Electrical Engineering department fellowship. This research was
843 supported by HHMI-Gates Faculty Fellows Grant (M.P.), NIH New Innovator Award (M.P.),
844 NSF Career Award (M.P.), NSF CCC (grant DBI-1548297) and Moore Foundation. **Author**
845 **contributions:** H.L. and M.P. designed the instrument and overall research. H.L. built and
846 characterized the instrument. H.L. collected data with assistance from M.P., L.V.F and

847 H.SM.. H.L. developed models for spectral imaging. L.F.V and M.V. developed the neu-
848 ral network for red blood cell segmentation. H.L., L.F.V and M.V. developed processing
849 pipelines and processed the data. H.SM and M.P performed field testing. H.L and M.P
850 wrote the manuscript. **Competing interests:** All authors declare no competing interests.
851 **Data and materials availability:** All data necessary for interpreting the manuscript have
852 been included. Additional information may be requested from the authors.

853 **Figures and Captions**

A The imaging platform



B Photograph of the prototypes

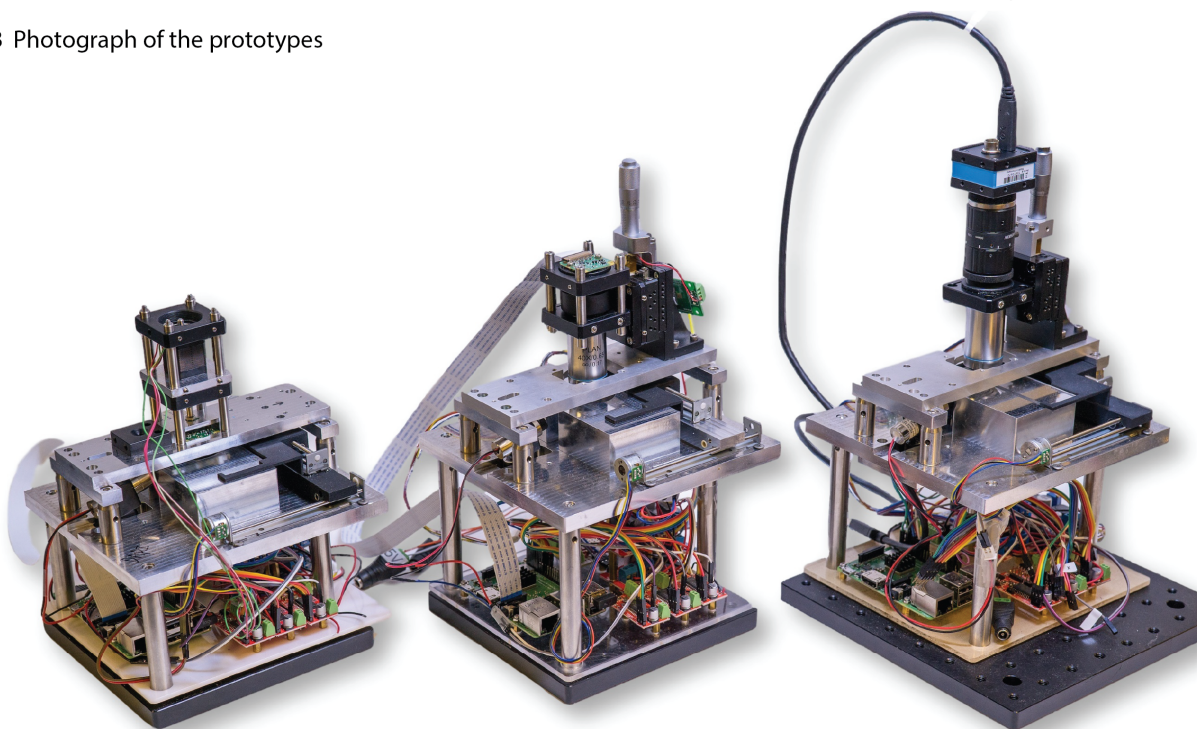


Figure 1

854 **Fig. 1. Reconfigurable high-throughput imaging platform. (A)** Construction of
855 the modular imaging platform. The left column shows three different imaging modules (top
856 row), a motorized scanning module, and three different illumination modules (bottom row).
857 In the *low mag imaging module* (top left), a captive linear actuator is used for focus actuation.
858 In the *high mag imaging module* (top middle and top right), piezoelectric stacks combined
859 with micrometers are used for focus actuation, where the micrometer can be replaced with
860 a captive linear actuator to motorize coarse adjustment. Inset shows the construction of the
861 low-mag imaging module sub-assembly, which consists of a pi-camera, a long pass interference
862 filter and another cellphone lens. For different applications, sub-assemblies with different
863 configurations should be switched as a whole, in contrast to the *high mag imaging module*,
864 where objectives, filters, tube lens and cameras can be individually switched. The right
865 column shows some examples of currently available portable computing devices that can be
866 used as the computation module. **(B)** A photograph showing three *Octopi* prototypes with
867 different imaging modules optimized for different applications.

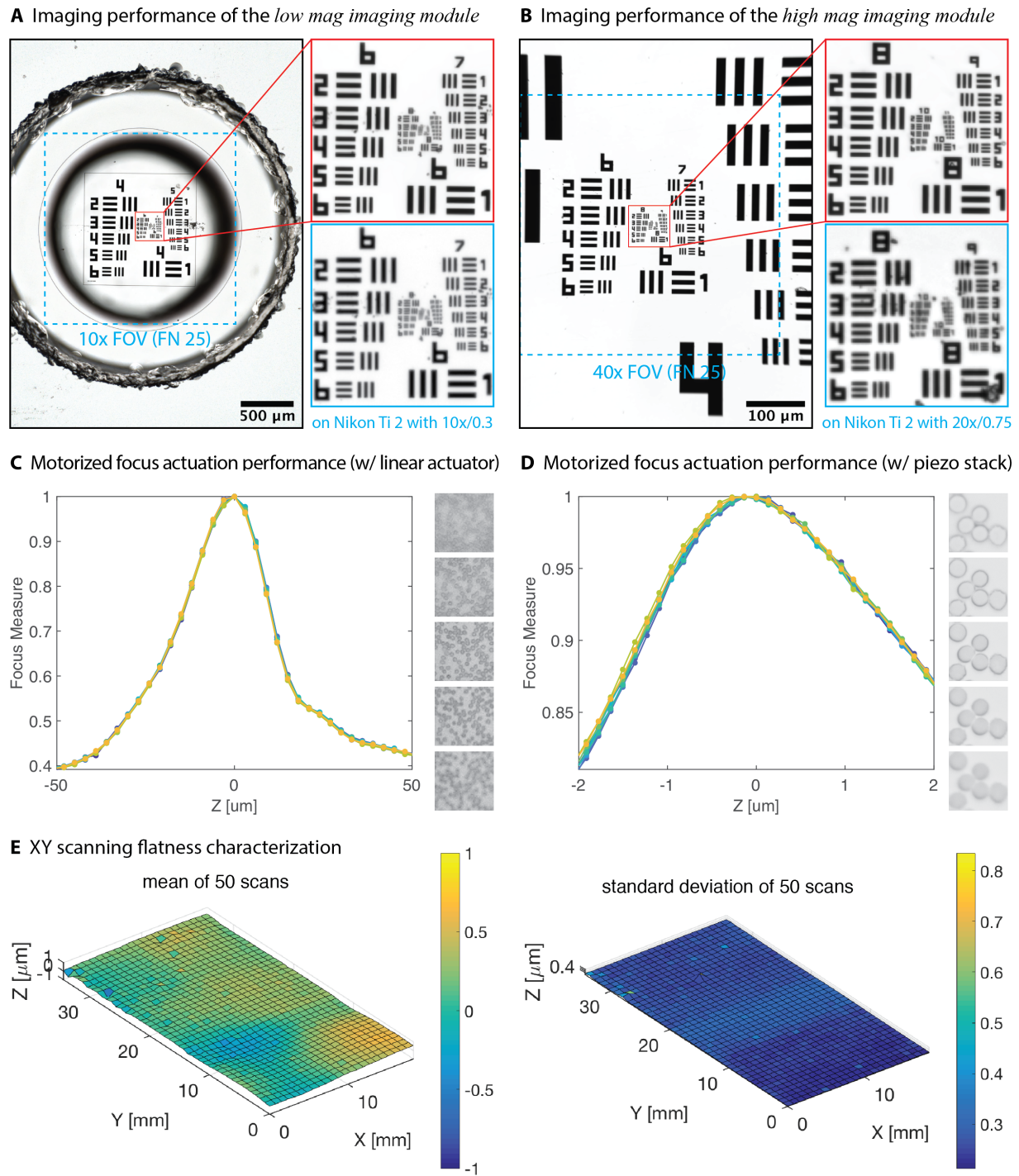
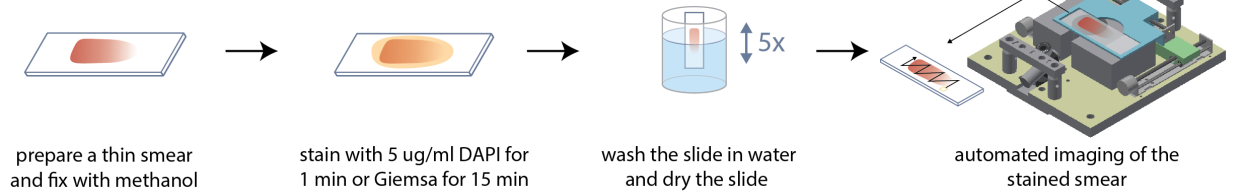


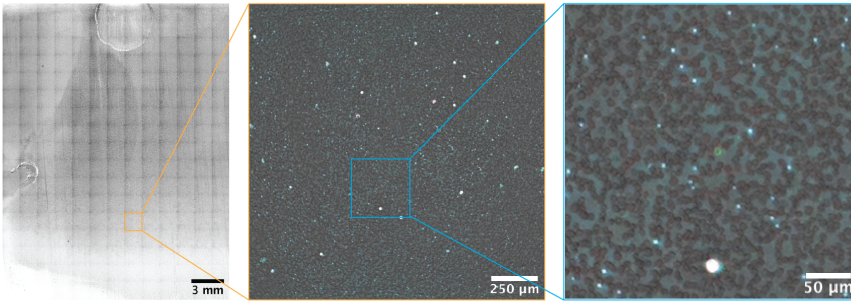
Figure 2

868 **Fig. 2. Characterization of the imaging platform.** (A-B) Images of a 1951 USAF
869 resolution obtained on *Octopi* with the *low mag imaging module* and the *high mag imaging*
870 *module* and their comparisons with images obtained on a Nikon Ti2 microscope. The image
871 obtained with the *high mag imaging module* (configured with 40x/0.65 objective) is better
872 resolved than its counterpart obtained on the Nikon Ti2 with an apochromatic 20x/0.75
873 objective and an additional 1.5x magnification because of its smaller object side pixel size
874 (0.202 μm compared to 0.367 μm). Images were denoised by a pretrained FFDNet denoiser
875 [93], see Fig. S13 for images before denoising. (C) Motorized focus actuation performance
876 of the *low mag imaging module* (using captive linear actuators) and the *high mag imaging*
877 *module* (using piezoelectric stacks). Plotted are focus curves (focus measure vs commanded
878 z position) for 10 repeated z-stacks. Step size of 3 μm and 137 nm is used for the captive
879 linear actuator and the piezoelectric stack respectively. The high degree of overlap between
880 the curves suggest reliable and repeatable focus actuation. Example images are 12 μm and
881 1.1 μm apart in z. (D) Characterization of XY scanning flatness for scanning module using
882 an ultra-flat glass slide. Mean and standard deviation of measured top surface z-positions
883 for 50 XY scans are plotted. The overall standard deviation is below 400 nm and is limited
884 by the measurement setup, suggesting excellent stage flatness. Similar result was obtained
885 with a normal microscope glass slide and plotted in Fig. S3.

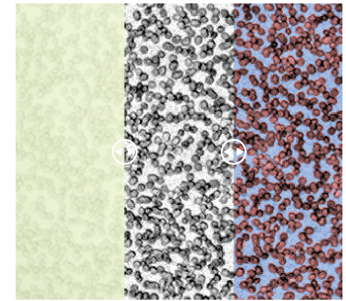
A Procedures for preparing and scanning a blood smear



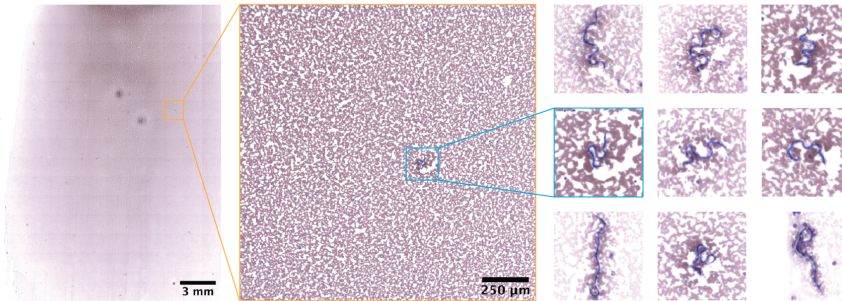
B Scan of a DAPI-stained blood smear



C RBC segmentation



D Scan of a Giemsa-stained blood smear with Loa Loa (African eye worm)



E Probability of occurrence

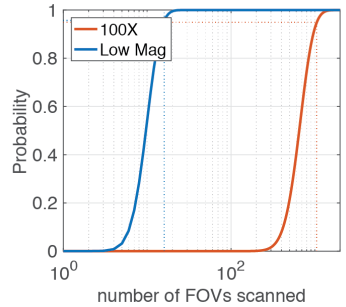


Figure 3

886 **Fig. 3. Blood smear examination.** (A) Procedure for preparing and scanning
887 a blood smear. (B) Scan of a DAPI-stained blood smear. From left to right: stitched
888 bright field images, a single FOV with overlaid bright field and fluorescent images, zoomed-
889 in overlay image with arrows pointing to (from top to bottom) a platelet, a reticulocyte and
890 a white blood cell. The smear is made from 4 μ l of blood and the region being imaged is
891 of size 20.8 mm x 27.2 mm (221 individual field of views), covering more than 90% of the
892 smear. With Raspberry Pi being used as the control & computation module, The scan took
893 19 minutes. This includes auto-focus using 20-plane z-stacks at the beginning and in the
894 middle of each row that accounts for about 1/3 of the total scan time. When implemented
895 with a control & computation module that has higher bandwidth (such as Jetson Nano),
896 shortening of the total acquisition time to below 4 minutes can be achieved. Besides, in
897 practice, digitizing a much smaller area of the blood smear is often sufficient. (C) Illustration
898 of steps for segmentation of red blood cells. Left to right: unprocessed portion, portion
899 with preprocessing applied (illumination correction and contrast adjustment), portion with
900 segmentation masked generated from a neural network overlaid. (D) Scan of a Giemsa-
901 stained blood smear with Loa Loa (African eye worm). The 9 zoomed-in images are of size
902 $188 \mu\text{m} \times 188 \mu\text{m}$ (E) Assuming parasitemia of 100 parasites/ul of blood, probability of
903 more than 10 parasites present vs total number of microscopic fields of view examined. The
904 two curves are for the *low mag imaging module* (field of view: 1.6 mm x 1.6 mm) and for a
905 100x objective commonly used for malaria diagnosis (field of view: 0.22 mm in diameter). In
906 the calculation, red blood cells is assumed to fill 75% of the field of views. For the probability
907 to be greater than 95%, on average more than 1058 of the 100x field of views need to be
908 examined, whereas only 16 low mag fields of view is sufficient.

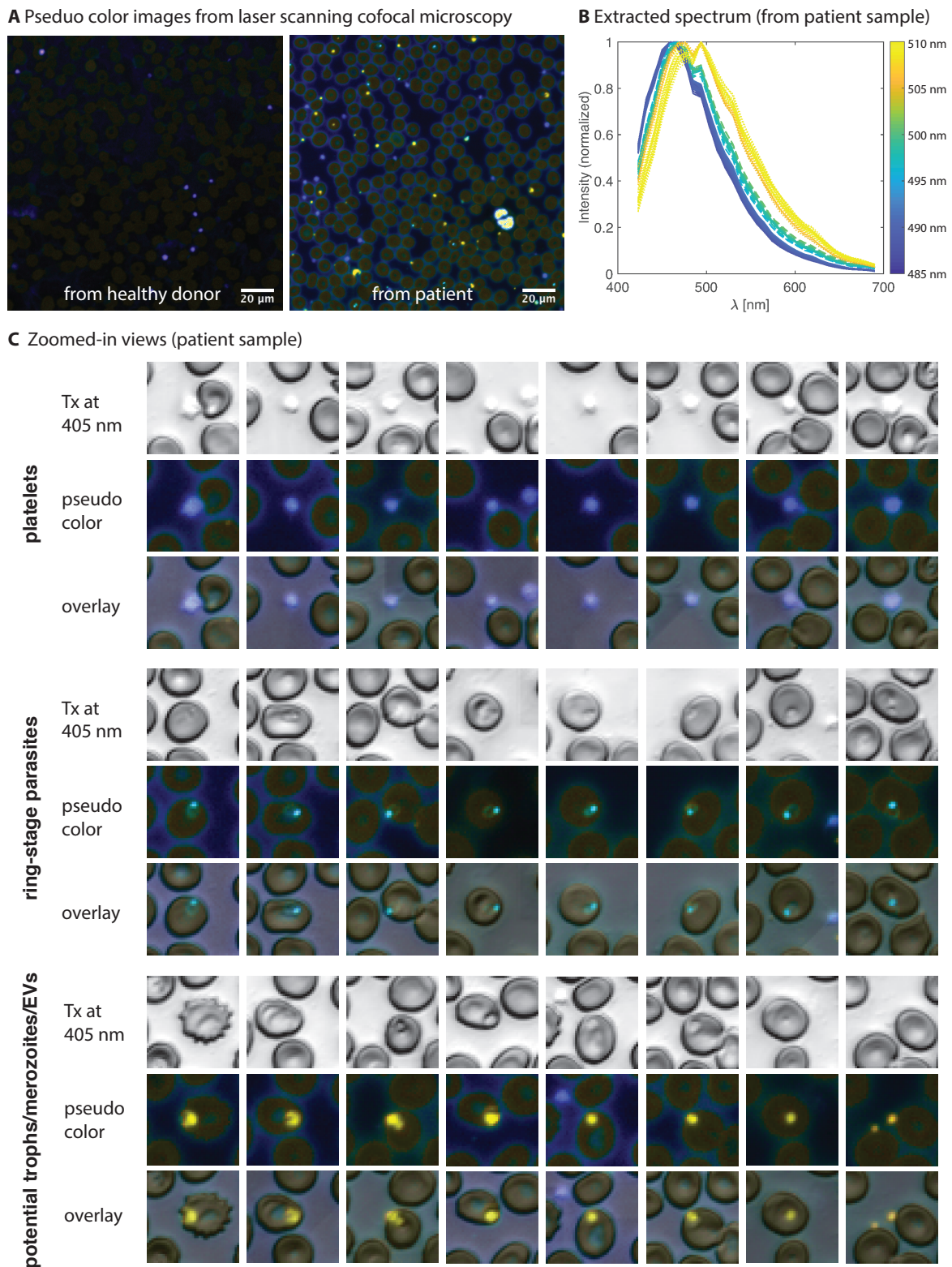
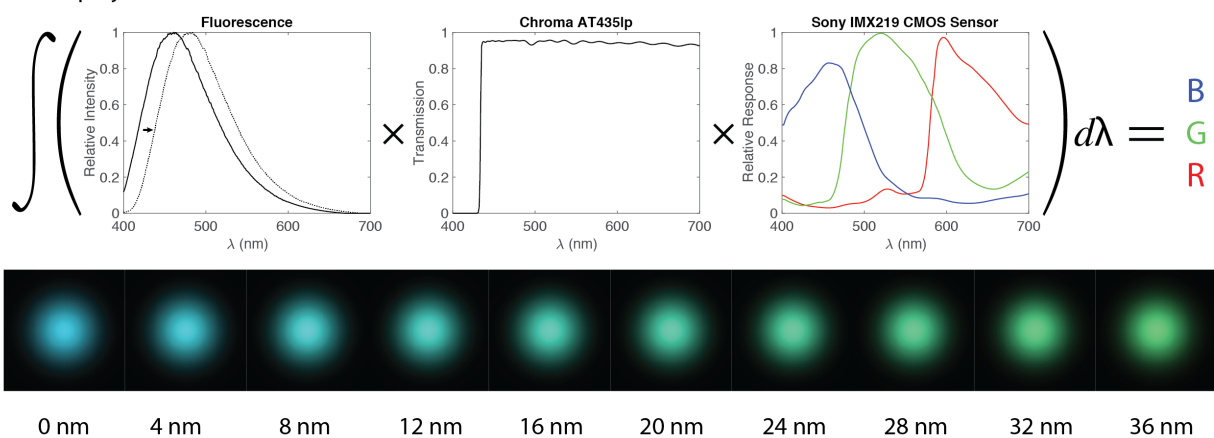


Figure 4

909 **Fig. 4. Spectral shift in DAPI-stained *P. falciparum* parasites.** (A) Pseudocolor images of DAPI stained blood smear from a healthy donor and from a patient diagnosed
910 with malaria. The images are acquired on a Zeiss LSM780 laser scanning confocal microscope
911 with a 20x/0.8 objective and 32 spectral channels. For each pixel, the color is determined
912 according to the centroid of the extracted 32-point spectrum for that pixel (B) Extracted
913 spectrum of selected fluorescent spots from image of the patient sample where each spectrum
914 is color-coded according to its spectral centroid in the same way as in (A). (C) Zoomed-in
915 views of platelets, ring-stage *P. falciparum* malaria parasites and potential *P. falciparum*
916 malaria trophozoites, merozoites and parasites-derived extracellular vesicles. Images are of
917 size $17 \mu\text{m} \times 17 \mu\text{m}$.
918

A RGB projection



B Simulation of fluorescent spots and their projections in the R/B - G/B space

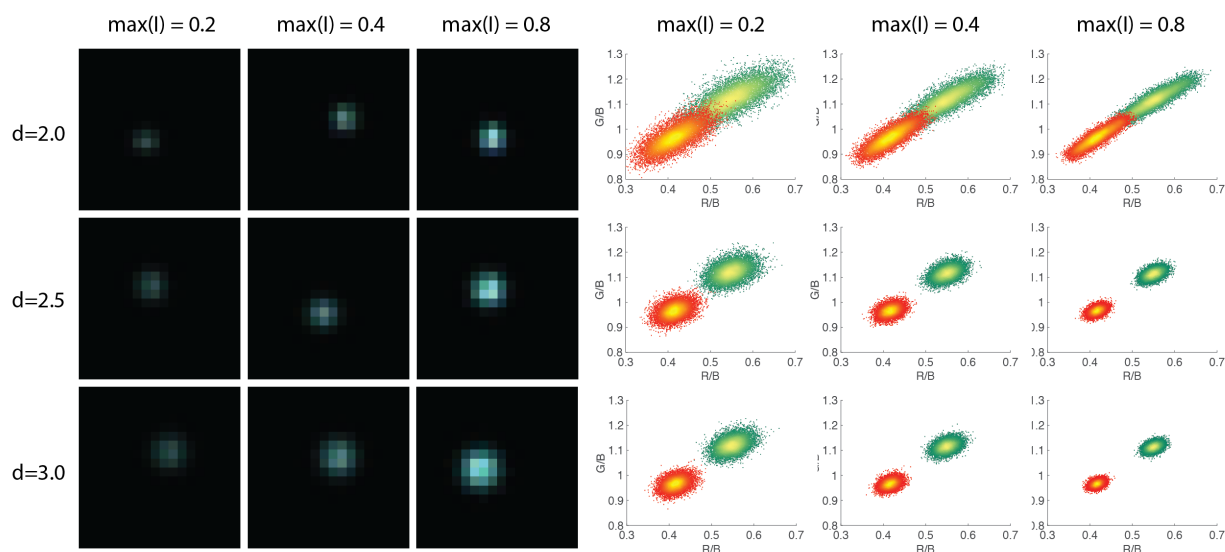


Figure 5

919 **Fig. 5. Simulation of three channel spectral imaging with an RGB CMOS**
920 **sensor. (A)** The process of converting spectrums to RGB values (top) and the resulting
921 colors for different amount of shift. The original spectrum without shift is the emission
922 spectrum from DAPI. **(B)** Example demosaiced images of simulated fluorescent spots of
923 different diameter and signal to noise level (left) and their projections in the R/B - G/B space
924 (right; the two clusters have spectral separation of 8 nm). For each parameter combination,
925 10,000 spots are randomly generated for each class. The spots are assumed to have Gaussian
926 profiles and the diameters are their RMS width. The signal level is the expected value of
927 the maximum pixel intensity of the spot. The number is normalized to have max value of 1,
928 which corresponds to the full well capacity of the CMOS sensor. In determining shot noise
929 for the pixel values, peak quantum efficiency conversion gain of the pi camera module is
930 used (peak QE: 70%, conversion gain: 0.2 e-/ADU). The shot noise is modeled by a Poisson
931 process. The position of spots are also randomized. For each spot, R/B is the ratio of total
932 red pixel intensity and total blue pixel intensity, and similarly G/B is the ratio of total green
933 pixel intensity and total blue pixel intensity. The R, G, B pixel values are directly taken
934 from the simulated raw Bayer data.

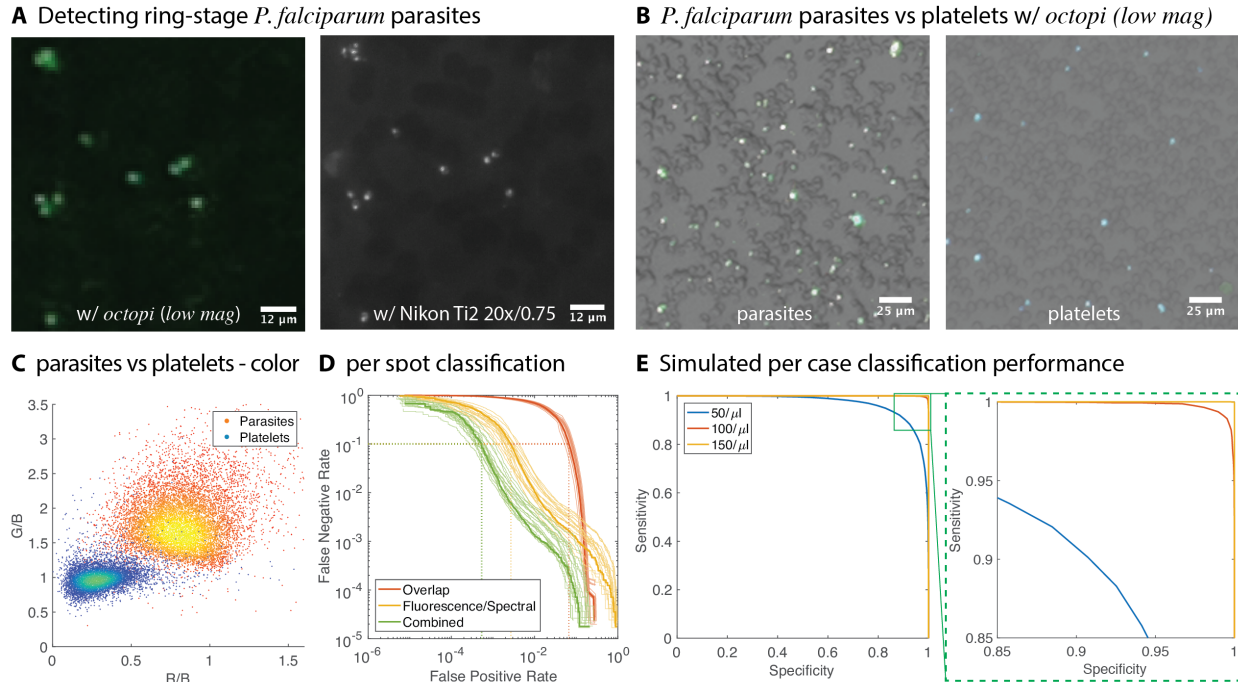
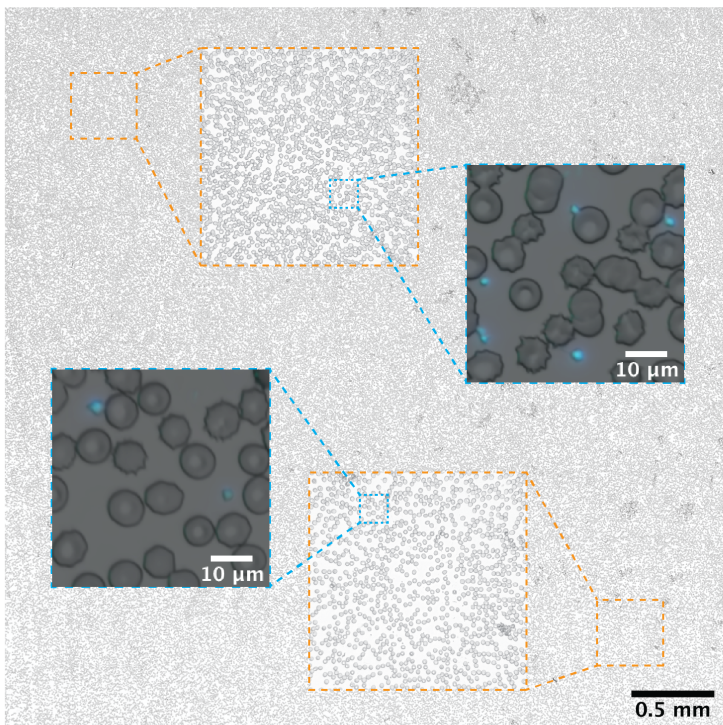


Figure 6

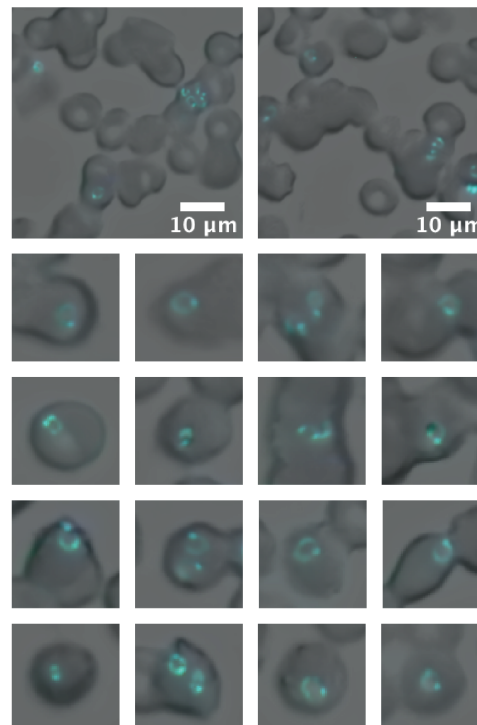
935 **Fig. 6. High throughput *P. falciparum* parasites detection at low magnifica-**
 936 **tion. (A)** Image of the same field of view of DAPI-stained smear of *P. falciparum*. culture
 937 obtained with the *low mag imaging module* on *Octopi* (left) and on Nikon Ti2, a high-end re-
 938 search grade microscope, with 20x/0.75 apochromatic objective (right). (B) Overlaid bright
 939 field and fluorescent images of DAPI-stained smears of *P. falciparum*. culture (left) and
 940 uninfected whole blood (right) obtained with the *low mag imaging module*. The color differ-
 941 ence of fluorescent spots in the two can be observed. We can also observe that the platelets
 942 are all outside right blood cells where as most parasites are inside the red blood cells. (C)
 943 Scatter plot of spots corresponding to parasites and platelets in the G/B vs R/B space. The
 944 spots are labeled according to whether they come from the *P. falciparum* culture smears or
 945 the uninfected whole blood smears. In the scatter plot, 10,000 randomly chosen spots from
 946 each class is shown. (D) Per spot classification performance for three different classes of
 947 classifier with 20-fold cross validation. The first classifier only uses features extracted from
 948 the fluorescent image for classification. The second classifier only uses the amount of overlap

949 between the fluorescent spot and the segmented red blood cells. The third classifier uses
950 both fluorescent features and overlap, which gives 0.05% false positive rate at false negative
951 rate of 10%. **(E)** Simulated per case classification performance assuming per spot FNR of
952 5×10^{-4} and FNR of 10%. 10,000 tests at each parasitemia level were simulated, assum-
953 ing examination of 0.5 μl blood (2.5 million red blood cells) per test. Each test outputs
954 an estimated parasitemia based on the number of red blood cells scanned and number of
955 parasites detected, and this number is compared with a decision threshold for determining
956 the outcome of the test. For each simulated parasitemia, this decision threshold is varied to
957 obtain the sensitivity vs specificity curve. We note that per case sensitivity and specificity is
958 a measure of performance at low parasitemia. For higher parasitemia (e.g., above 200/ μl),
959 estimated parasitemia may be directly used. Compared to RDT, the ability to quantify
960 parasitemia is a strength of microscopy and is useful for evaluating disease severeness and
961 monitoring treatment response.

A Large area scan of blood smear (uninfected whole blood)



B *P. falciparum* lab culture



C *P. falciparum* malaria patient blood smear

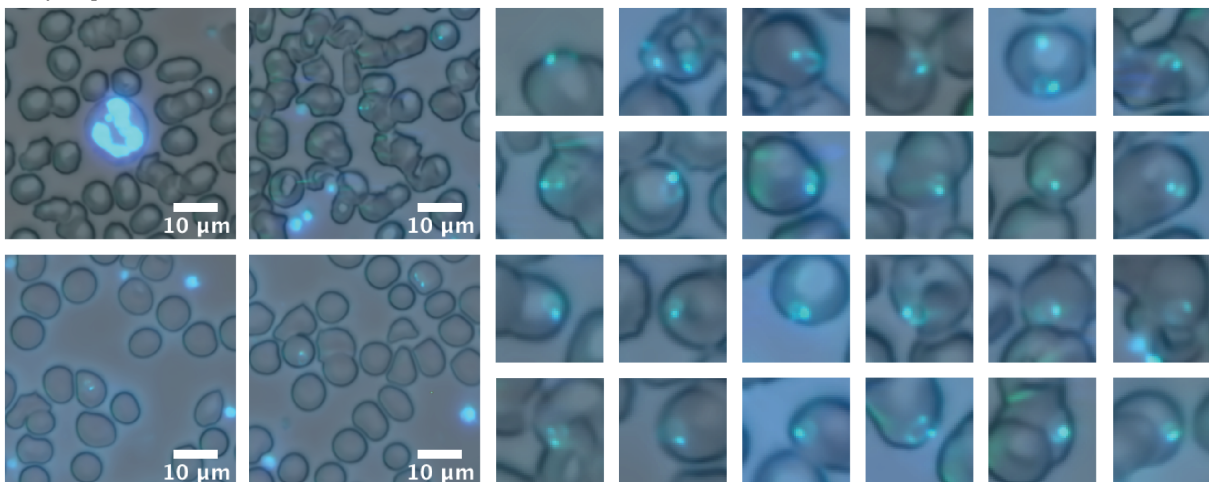
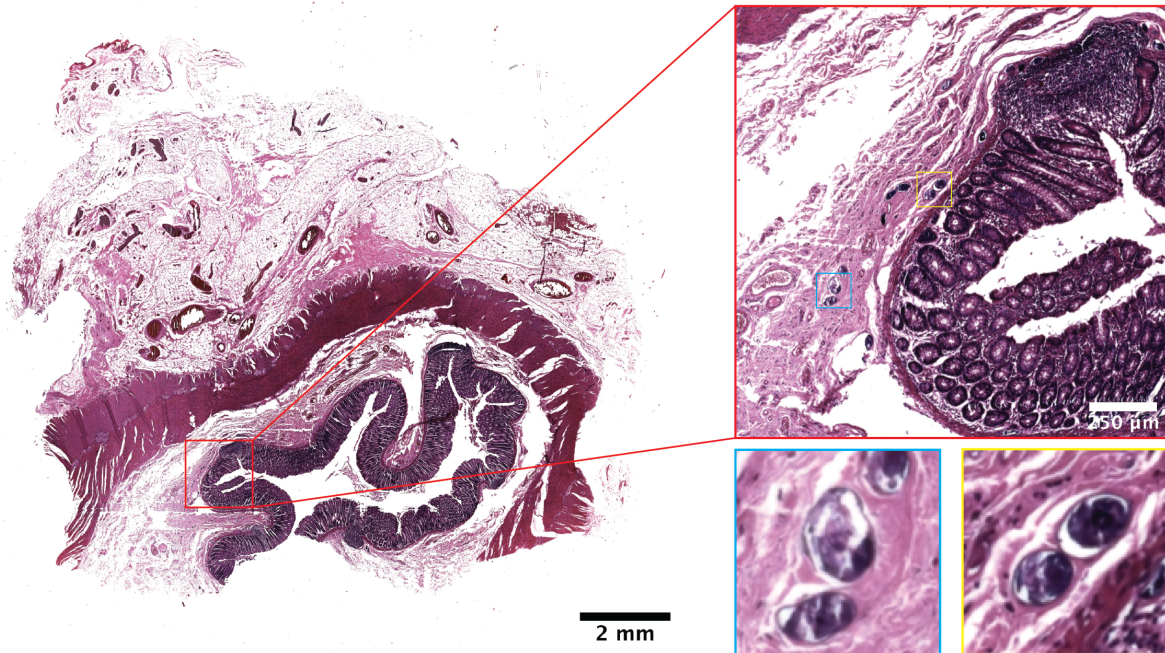


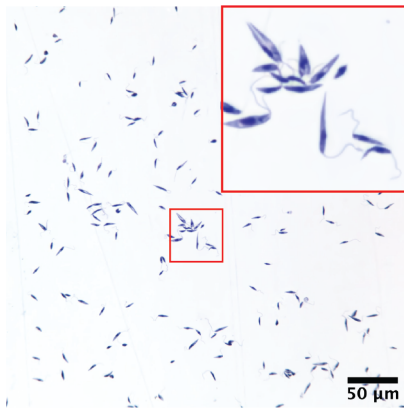
Figure 7

962 **Fig. 7. Imaging Blood Smear with the *high mag imaging module*.** (A) A 11
963 \times 11 FOV (4.4mm \times 4.4mm) scan of DAPI-stained blood smear of a healthy individual.
964 Platelets are visible in the zoomed-in overlaid bright field and fluorescent images (B) Selected
965 field of views showing red blood cells infected with ring-stage parasites. Some red blood cells
966 are infected with multiple red blood cells. Ring like morphology of the parasites is clearly
967 visible (C) Patient sample showing a white blood cell (top left), platelets and infected red
968 blood cells. Each close-up image in (B) and (C) is of size of $12.9 \mu\text{m} \times 12.9 \mu\text{m}$. Images were
969 denoised by a pretrained FFDNet denoisiser [93], see Fig. S13 for images before denoising.

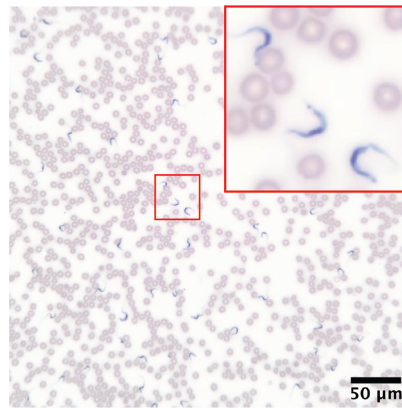
A Schistosomiasis of Intestines



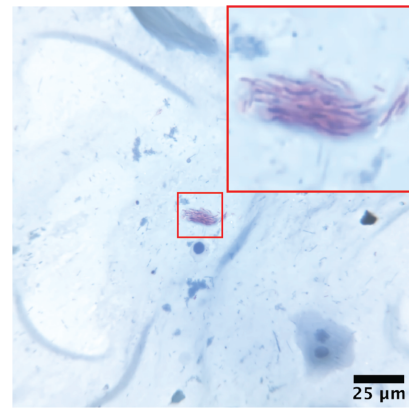
B Leishmania donovani



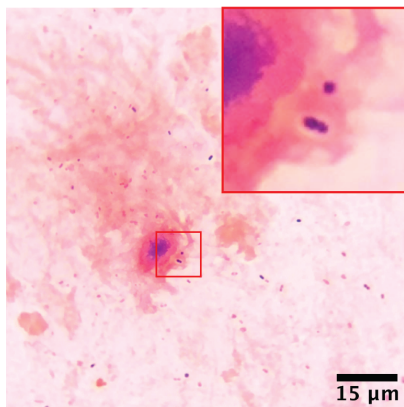
C Trypanosoma brucei rhodesiense



D Mycobacterium tuberculosis



E Streptococcus pneumoniae



F Staphylococcus aureus

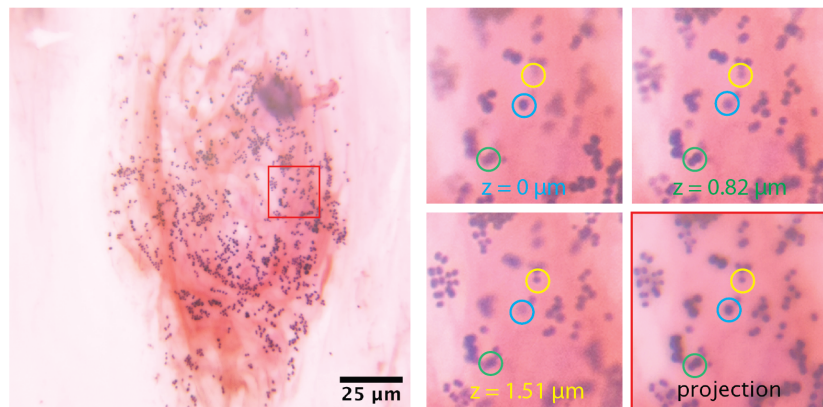


Figure 8

970 **Fig. 8. Other diagnostic applications for *Octopi*.** (A) H&E stained Schistosomia-
971 sis of intestines specimen obtained with the *low mag imaging module*. Close-up images show
972 eggs of *Schistosoma haematobium*. (B) Hematoxylin stained promastigotes of *Leishmania*
973 *donovani* obtained with the *high mag imaging module* using a 40x/0.65 Plan Achromatic
974 Objective. (C) Giemsa stained *Trypanosoma brucei rhodesiense* in a thin blood smear ob-
975 tained with the *high mag imaging module* using a 40x/0.65 Plan Achromatic Objective.
976 (D) ZiehlNeelsen stained *Mycobacterium tuberculosis* in a sputum sample obtained with the
977 *high mag imaging module* using a 100x/1.25 Plan Achromatic Objective. (E) Gram stained
978 *Streptococcus pneumoniae* in a sputum sample obtained with the *high mag imaging module*
979 using a 100x/1.25 Plan Achromatic Objective. (F) Gram stained *Staphylococcus aureus* in a
980 sputum sample obtained with the *high mag imaging module* using a 100x/1.25 Plan Achro-
981 matic Objective. Left shows minimum intensity projection of a z-stack containing 20 planes
982 with z-step size of 137 nm. Right shows close-up images of different z-planes and the min-
983 imum intensity projection corresponding to the same field of view. Images in (A)-(D) were
984 denoised by a pretrained FFDNet denoiser [93], see Fig. S13 for images before denoising.

985 List of Supplementary Materials

986 Fig. S1. CMOS sensor characterization and anticipated performance.

987 Fig. S2. Setup for scanning stage flatness characterization.

988 Fig. S3. Characterization of XY scanning flatness for scanning module using a normal
989 microscope glass slide.

990 Fig. S4. Per frame processing time of Top-hat transform and LoG Spot detection imple-
991 mented on different computation modules.

992 Fig. S5. Illustration of the spot detection pipeline.

993 Fig. S6. Deep learning red blood cell segmentation.

994 Fig. S7. Full field of view pseudo color image of uninfected whole blood.

995 Fig. S8. Full field of view pseudo color image of blood smear from patient diagnosed of
996 *P. falciparum* malaria.

997 Fig. S9. Parts common to different configurations of *octopi* presented.

998 Fig. S10. Training of the convolutional neural network.

999 Fig. S11. Features used by the classifier and their importance scores output by the
1000 classifier in the training phase.

1001 Fig. S12. Empirical distribution of overlap between red blood cells and *P. falciparum*
1002 parasites

1003 Fig. S13. Images before and after denoising.

1004 Table S1. Cost breakdown for *Octopi*.

1005 Movie S1. Operation of the *Octopi* platform for automated slide scanning.

1006 Movie S2. Focus adjustment with Piezo actuator while imaging a resolution target.